TECHNOLOGICAL EDUCATIONAL INSTITUTE OF CRETE

BRANCH OF CHANIA

DEPARTMENT OF ENVIROMENTAL AND NATURAL RESOURCES ENGINEERING

Bachelor Thesis

"Comparing RST-FIRES and MOD14 algorithms for detecting forest fires in Attica and Crete"

KOMINOU CHRISTINA-EFSTATHIA

Supervisor(s) Professor(s)

Prof. Valerio Tramutoli

Prof. Fillipos Valianatos

Dr. Carolina Filizzola

Dr. Theodosio Lacava

UNESCO Chair
SOLID EARTH PHYSICS and GEOHAZARDS RISK REDUCTION
Technological Educational Institute of Crete, Greece
Head of the Chair, Dr. Filippos Vallianatos
Professor of Geophysics & Seismology
3 Romanou Str., Chania, GR 73100, Crete, Greece. email : fvallian@chania.teicrete.gr

Acknowledgements:

This study was made during my Erasmus Placement in University of Basilicata in Potenza, Italy. I would like to express my deepest gratitude and appreciation to my professor from Technological Educational Institute of Crete Filippo Vallianato for giving me the opportunity to fulfill my studies for the last semester in Italy. My deepest gratitude to my supervisor Prof. Valerio Tramutoli who accepted my application for my placement and also for his continuous help, advice and inspiration for this study. Also I am really thankful and I would like to give my sincere thanks to Teodosio Lacava and Carolina Filizzola for their guidance , they were always there to answer my questions and help me with any problem that I had.

ΠΕΡΙΛΗΨΗ

Οι δασικές πυρκαγιές αποτελούν σήμερα το πιο γνωστό κοινό πρόβλημα που αντιμετωπίζουν τα δάσοι μας και το φυσικό περιβάλλον. Στην παρούσα πτυχιακή, πραγματοποιήθηκε σύγκριση μεταξύ των αλγορίθμων RST-FIRES και MOD14/MYD14 για Αττική και Κρήτη, οι οποιοι για πρώτη φορά εφαρμόστηκαν σε δεδομένα MODIS. Αρχικά κατέβηκαν δεδομένα για τον Ιουλιο του 2003 εως 2015 τα οποία ηταν διαθέσιμα από το Institute of Methodologies for Environmental Analysis (IMAA) of the National Research Council (CNR), Tito Scalo (PZ). Τα δεδομένα MODIS για τις περιοχές ενδιαφέροντος και συγκεκριμένα για τον Ιούλιο 2007 τα οποία δεν ήταν διαθέσιμα από το IMAA-CNR πάρθηκαν απο το LAADS (Level 1 and Atmosphere Archive and Distribution System).

Μετα την σύγκριση των δυο αλγορίθμων και αφου επεξεργάστηκαν 194 καταγεγραμμένες πυρκαγιές για Αττική και Κρήτη, διαπιστώθηκε οτι ο RST-FIRES ειναι πιο ευαίσθητος στον εντοπισμό πυρκαγιών σε σχέση με τον MOD14/MYD14. Συγκεκριμένα ο RST-FIRES στην ταυτοποίηση πυρκαγιών παρουσίασε 31% επιτυχία για την Αττική και 30% για την Κρήτη. Αντίθετα, ο MOD14/MYD14 παρουσίασε 27% επιτυχία για την Αττική και 24% για την Κρήτη.

ABSTRACT

Forest fires are currently the best known and common problem facing the forest and the natural environment. In this thesis MOD14/MYD14 algorithms have been compared with RST-FIRE, for Attica and Crete, which has been for the first time applied on MODIS data. Firstly, all data that acquired in July from 2003 to 2015 were available in the on-line archive of the Institute of Methodologies for Environmental Analysis (IMAA) of the National Research Council (CNR), Tito Scalo (PZ). Specifically, for the areas of interest and the year of validation (July 2007), MODIS data that were not available in IMAA-CNR archive were downloaded from LAADS (Level 1 and Atmosphere Archive and Distribution System) (https://ladsweb.nascom.nasa.gov/).

After the comparison of two algorithms and from processed of 194 documented events for Attica and Crete, RST-FIRES appeared to be more sensitive than MOD14/MYD14. Specifically, the RST-FIRES in identifying fires showed 31% success for Attica and 30% for Crete Island. Instead, the MOD14 / MYD 14 showed a 27% success for Attica and 24% for Crete Island.

Contents

Introduction

Fires are one of the main disturbances that affect terrestrial ecosystems and have profound consequences on global climate, air quality, and vegetation structure and functioning. In Europe alone, fires impact more than half a million hectares of forest every year. Fire regimes are determined by climate, vegetation, and direct human influence. Climate is recognized as the major determinant of fire patterns on a global scale. In Europe, human activities including negligence and arson cause more than 95 % of European forest fires. At the same time, overall trends are closely linked to weather conditions, with the sub-humid and arid areas that are particularly prone to large wildfires. Among the European countries, the Greece has experienced a tremendous increase in the number of forest fires in last 35 years, with a consequent escalation in the number and size of the burned area. The huge emergency occurred during the summer of 2007, with dozens of victims and incalculable damage, is well representative of the severity of the situation.

Besides implementing adequate prevention measurements, a timely identification of fires can drastically reduce their potential effects, allowing the rapid intervention of specific countermeasures. A number of techniques can be used for fire detection, but the ones based on satellites data present few advantages in terms of operational and economical perspectives. Owing to a satellite synoptic view, they can be used to monitor very large areas, with relatively low cost. Moreover, geostationary satellite as well as constellation of more polar meteorological satellites can provide high data acquisition frequency which is critical for quick and real-time fire detection and monitoring.

The Moderate Resolution Imaging Spectroradiometer (MODIS) on board both of Aqua and Terra satellites is one of the sensors most used for forest fire detection. Indeed it is able to acquire data in the Medium Infrared (MIR) spectral range, the one more sensitive to hot spot sources like fires, with a medium spatial resolution (1 km) and a good temporal resolution (4 images per day). Thanks to these characteristics, different algorithms for forest fires detection have been developed so far. Among them, the MOD14/MYD14, one, developed at NASA, is one of the most used at a global level. This algorithm is separated by levels and also the outputs are daily provided by NASA. The Level 2G, Level 3 and Level 4 products were the most important for the analysis, are defined on o global 250 m (172800 x 86400 pixels), 500m or 1km (43200 x 21600 pixels), sinusoidal grid and they are divides into fixed approximately 10^0 x 10^0 in size. Each tile (Giglio, 18 February

2010) is assigned a horizontal (H) and vertical (V) coordinate, ranging from 0 to 35 and 0 to 17, respectively.

In this thesis MOD14/MYD14 algorithms have been compared with RST-FIRE, which has been for the first time applied on MODIS data. Specifically, the Robust Satellite Techniques (RST), (RST Tramutoli, 2005, 2007) is a general technique for the analysis of satellite data which have been already successfully applied for the investigation of different natural and environmental processes occurred on the Earth's surface. This algorithm is based on the analysis of multi-year historical series of homogeneous satellite records for the identification of signal normal behavior pixel level. All the analyzed data, acquired in July from 2003 to 2015, were available in the on-line archive of the Institute of Methodologies for Environmental Analysis (IMAA) of the National Research Council (CNR), Tito Scalo (PZ).

The information about the fires occurred in Attica and Crete during July 2007 have been used has reference for comparing the output of the algorithms. In order to produce these outputs, few pre-processing routines were implemented. First, it was necessary to fill the IMAA archive with the data not available, downloading them from LAADS (Level 1 and Atmosphere Archive and Distribution System - https://ladsweb.nascom.nasa.gov/). About YYYY MODIS data have been analyzed in this work. All data were calibrated in terms of reflectance (VIS, channel 01) or brightness temperature (MIR, channels 21, 22; TIR, channels 31, 32). For each image, sensor zenith information was extracted, too.

The thesis is organized as follows: the first chapter will provide a brief introduction on fire forest especially on danger of fire forest in season 2007. In second chapter the basic physical principles of Remote Sensing and how Remote Sensing Techniques are useful for fire forest detection, are described. Third chapter presents the Robust Satellite Techniques (RST) and MOD14/MYD14 algorithms approaches for fire detection. In the fourth chapter the achieved results will be analyzed and discussed in detail for Crete Island and Attica for July 2007.

CHAPTER 1
FIRE FOREST IN GREECE

1.1 Forest and Fires

The forest is one of the most complex ecosystems in nature. From ancient times to our days, forest ecosystems play an essential and decisive role in safeguarding the global ecological equilibrium. It is however, currently a fact that forest is not only one of the greatest and most overland natural ecosystems but also goods among the most vulnerable.

The importance of the forest is self-evident. It is the primary regulator of global climate, it produces oxygen and contributes to tackling climate change, by holding important quantities of carbon dioxide. It constitutes rich ecosystems of enormous importance, complex biotope, which host important variety of flora and fauna. It is a key link in the hydrological cycle, increasing the permeability of territories and retaining important natural water quantities.

The main risk for the forests is wildfires. Wildfire is an uncontrolled fire in an area of combustible vegetation that occurs in the overhang (i.e., not in an urban area). Depending on the type of vegetation that is burnt, a wildfire can also be classified as abash fire, forest fire, desert fire, grass fire, hill fire, peat fire, vegetation fire, or veldt fire.Furthermore, differs from other fires by its extensive size, the speed at which it can spread out from its original source, its potential to change direction unexpectedly, and its ability to jump gaps such as roads, rivers and fire breaks. They can be qualified in terms of the cause of ignition, their physical properties such as speed of propagation, the combustible material present, and the effect of weather on the fire.

As a matter of fact wildfires occur when all of the necessary elements of a fire triangle come together in a susceptible area, an ignition source is brought into contact with a combustible material such asflora, which is subjected to sufficient heat and has an adequate supply of oxygen from the ambient air. High moisture content usually prevents ignition and slows propagation, because higher temperatures are required to evaporate any water within the material and heat the material to its fire point. Dense forests usually provide more shade, resulting in lower ambient temperatures and greater humidity, and are therefore less susceptible to bonfires. Notably less dense material such as grasses and leaves are easier to ignite because they contain less water than denser material such as branches and trunks. Plants continuously lose water by evaporation of water and transpiration from plants, but water loss is usually balanced by water absorbed from the soil, humidity, or rain. Often a consequence of droughts is when this balance is not maintained; plants are dry and therefore are

more flammable. Whether the change is taking place, the final destruction depends largely on the prevention measures taken by the people.

1.1.1 Causes, consequences and frequency of forest fires.

The causes of forest fires have different origin. As it is known, the biggest disasters are caused by humans. Many of these forest fires are caused by cigarette butts being left on the land, campfires that have been left unmonitored, as well as intentional acts of arson.Someman-made causes of forest fires are described in the following:

- **Burning Debris:** It is pretty common to burn yard waste in many places. Even when it is legal to do so, it may cause fires at many places when things go out of hand. Winds play a major role in wildfire. They can cause flames of burning debris to spread into forests or farms or fields.
- **Unattended Campfires:** Camping can be of great fun for both young and old age people. Unattended campfires can put things out of control and can cause forest fire. It is therefore recommended to choose safe location for a campfire that is away from ignitable objects and is stocked with a bucket of water and a shovel.
- **Equipment Failure or Engine Sparks:** A running engine can spew hot sparks when things go wrong. Car crashes have been known to start fires quickly and that is why it is common to see firefighters rush to the scene in anticipation of a fire. Small engine sparks can give way to high flames if that vehicle is operating in a field or a forest.
- **Cigarettes:** Cigarettes are another common cause of forest fires. It is common for people to throw the cigarette bud on the ground knowing that it is still burning. Smokers must understand that a small negligence on their part can cause huge impact on the environment and surrounding areas.
- **Fireworks:** Fireworks are fun to shoot off but special care needs to be taken when they are in the hands of amateurs. Fireworks must be avoided even when there is small chance that they could start a wildfire. If not handled properly that may end up as flames in unwanted territory.
- **Incediarism:** incediarism is the act of setting fire to property, vehicles or any other thing with the intention to cause damage. A person who commits this crime is called an incendiary. Incediarism is sometime done by people to their own property in order to receive compensation and may account for 30% of all forest fires cases.

On the other hand, a lesser liability percentage of 3%, Mother Nature's also responsible of forest fires in Greece. The most important cause is lightening, especially the type of lightning called "hot lightning", which can last for a relatively long time. When it strikes, it can produce a spark which can set off a forest or a field.

Clearly, the overwhelming proportion of forest fires comes from the human and in particular, the human volition or indifference.

Forest fires also cause many effects. If you have ever seen firefighters battling a forest fires and the images they show on TV, it will give you an idea of the immediate damage fires forest can do to flora. Fires also destroy houses and almost anything in its way. Additionally, the city spends millions of money to fight them with chemicals, logistics, aircrafts and trucks, time and personnel. The economic loss can be huge. One more effect is the soil sand organic matter. Forest soils are rich in decaying debris and nutrients, and are composed of many natural features that support a myriad of life forms and organic activities. The fire raises the temperatures of these soils to over 900°C and this potentially wipes away almost all the organic value of the soil.The effect on watershed is also important. Burned organic matter in the soil (volatized organic compounds) also affects the natural layering of the soils. This negatively affects infiltration and percolation, making the soil surfaces water repellent. Water therefore is unable to drain into water tables and the run-offs on the surfaces cause erosion.

Forest fires occur in our country even the most destruction, to have approximately 80% in the period from 1st June until 31 October, although it is not rare fires in some areas during November or May, particularly during the dry years. During the 24 hours approximately 90% of them occur between 08:00 and 23:00, with maximum, between 14:00 to 17:00. This phenomenon has clear relationship with the daytime running of variation of relative humidity.

1.2Fire danger in 2007 season.

In recent decades, the extensive forest fires are the strongest and most dense factor cumulatively upset the natural balance of Greek space. They constitute the effects of aging with devastating frequency and intensity, in a predominantly igneous and flammable natural environment as regards climate and vegetation.

We will focus on 2007, which has been the worst year for forest fires ever recorded in Greece. The paragraphs below describe some unusual characteristics of the 2007 fire season that contributed to making it so extreme.

Weather conditions:

- Three unusually long periods of extremely high temperatures causing conditions of prolonged heat waves.
- Prolonged drought in the past months.
- Simultaneous strong winds blowing in the regions where the fires started.

The characteristics of the three consecutive heat waves were:

- Very high maximum temperatures (in some areas above 46o C).
- Very high minimum temperatures during the evening.
- Very low levels of humidity.
- The heat waves were followed by very dry and strong Northern winds.

The major fires broke out after the three consecutive heat waves, while their increasing size was a result of the extreme drought and hot conditions coupled with very strong winds, especially in last week of August in Peloponnesus. At the end of August, five major fires in Peloponnesus burnt a total of 170 000 ha, two other major fires at the same time in Evia burned 25 000 ha of land, More than 70% of the final total burnt areas in the season resulted from the above 7 forest fires.

1.2.1Examples of large fire causes

June

The first major fire of the summer of 2007 was started on 28 June 2007. It is perceived to have been started by either an exploding electrical pylon or by arsonists. Significant parts of the Parnitha National Park were destroyed (Figure 1.1), and in total, the fire burnt 15,723 acres (63.6 km^2) of the core of the national forest in a matter of days. Overall the mountain of Parnitha suffered a burnt area of 38,000 acres (153.8 km^2), making it one of the worst recorded fire forest in Attica since the Penteli fire of July 1995. The magnitude of the devastation was unforeseen. Environmental studies in Greece report that the Athenian microclimate will significantly change to warmer during the summer season, and inundation is now a very probable danger for the northern suburbs of the city. Mount Parnitha was considered the 'lungs' of Athens, following its considerable burning, both the city and local flora and fauna are expected to feel the consequences. Other affected areas included Pelion, Agia and Melivoia, Skourta, Dafni, and Pyli

Figure 1.1: View of the Parnitha National Park fire from north Athens (Source: https://en.wikipedia.org/wiki/2007_Greek_forest_fires)

July

On 11 July 2007, another fire sparked at a garbage dump near Agia Paraskevi, Skiathos, and spread across the island. Residents and tourists were forced to evacuate to nearby Troulos, and returned after the fire was put out. More than 100 fires were reported by 15 July 2007, in such locations as Kerateaoutside of Athens, Peloponnese, and on the Aegean islands of Andros, Evia, Lesbos, and Samos, as well as Crete and the Ionian island of Kefalonia. In Peloponnese around 20 July 2007, a fire which started from the mountains over the town of Aigio expanded rapidly towards 24 July 2007 Diakopto and Akrata, destroyed a large area of forests and cultivated land. In the same fire many villages were totally or partially burned, resulting in the loss of 230 houses and 10 churches, three people lost their lives. A 26-year-old farmer and a 77-year-old woman were arrested on suspicion of arson concerning the fires in Aigio(Figure 1.2) and Diakopto. The farmer confessed and is currently held in prison.

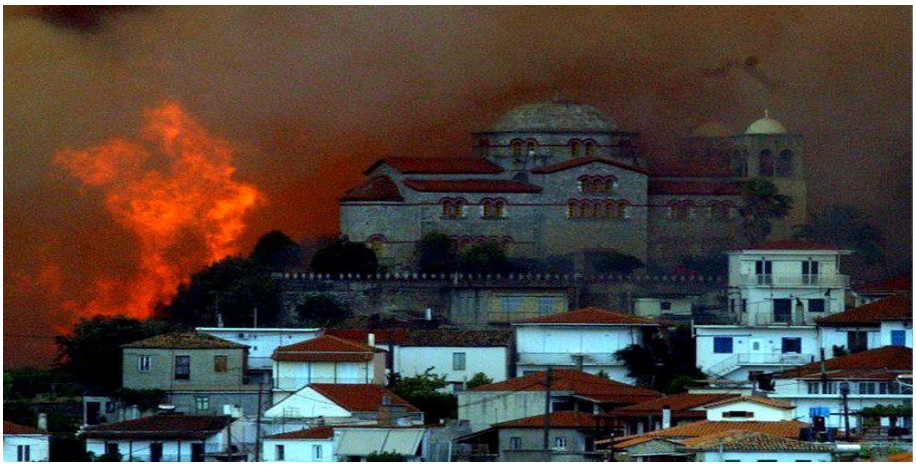

Figure 1.2.: Fire forest in Aigio. (Source: http://egionews.blogspot.it/2013/07/24-2007.html)

August

Fires continued, on 16 August 2007 they started to burn on the outskirts of Athens. The fire started on Mt. Penteli began burning down towards the suburbs (Figure 1.3). More than sixty fire engines, nineteen planes and helicopters, and hundreds of firefighters as well as locals attempted to hold back the fire. Melisia, Vrilisia, and Penteli city were affected in the blaze that was put out once winds calmed down. On 24 August 2007, fires broke out in Peloponnese, Attica and Euboea. In Peloponnese, the fire burnt many villages and accounted for 60 deaths. Six people were reported to have been killed in the town of Areopoli. In Zacharo, one of the worst hit areas, more than 30 people were found dead by firefighters while searching burning cars and homes. On 25 August 2007, fires broke out on Mount Hymettus and in the suburb of Filothei in Athens. Officials said these fires were the result of arson, as the firefighters found many bottles with gasoline in affected areas. Arson is also suspected for the fires in Peloponnese, as more than 20 fires started at about the same time. Moreover, two fires broke out in Keratea and one in Markopoulo Mesogaias in East Attica on 25 August 2007. The first fire was not under control until the following day, while the second was put out quickly. The Keratea fire had a length of 12 kilometres (7 mi) and a man was hospitalized with second degree burns. The fire at Lagonissi was reported as an accident, as it was started when a man accidentally set fire to a tree in his garden.

Figure 1.3: Forest fire in Penteli on 16August
(Source:https://en.wikipedia.org/wiki/2007_Greek_forest_fires)

September

The fires continued to burn into early September. On 1 September 2007, firefighters were still suppressing a strong blaze in Peloponnese (Figure 1.4). Three blazes remained, with the fires

destructive path continuing in Arcadia and Mt. Parnon in Laconia. Then, on 3 September 2007 a lightning strike started a new fire on Mt. Vermion, which was soon brought under control by firefighters. On 5 September the death toll reached 67, and on 21 September reached 68.

Figure 1.4: Fire forest in Peloponnesus (Source: https://www.google.com.pg/search?q=forest+fires+in+peloponnisos+2007)

As a result of the catastrophic events:

- 1 710 buildings burned down or were rendered uninhabitable
- Many villages were evacuate
- Several protected (Natura2.000) sites were destroyed
- Sites of major international interest, such as Ancient Olympia, were threatened
- A large scale economic and social damage to the rural economies occurred.

1.3 Firefighting means and information campaigns

The following ground and aerial means of the Greek government participated in the forest fire fighting operations. The total personnel of the Fire Brigade was about 14 500 from which 9 500 is permanent personnel which deals also with the structural fires and 5 500 is the seasonally hired personnel just for the forest fires. Fire Brigade of Greece owns about 1.525 engines, which are involved in both structural and forest fire suppression efforts and few more small engines owned by Municipalities of high risk areas involved occasionally in some incidents. The suppression efforts were supported also by:

- 3000 Soldiers.

- 200 Volunteers of Fire Services
- Hundreds of Volunteers
- Hundreds of active Citizens.

Also, the following aerial means were operating for the fire fighting operations:

- 21 CANADAIR fire fighting aircrafts
- 18 PZL fire fighting aircrafts
- GRUMMAN fire fighting aircrafts
- SUPER PUMA helicopters
- BK-117 helicopters
- 19 special fire-fighting helicopters
- 1 Be-200 fire fighting aircraft

Besides the above, upon request, provided to Greece assistance from the members of the European Union and other nations. Which were Austria, Canada, Croatia, Cyprus, Czech Republic, Denmark, Finland, France, Germany, Hungary, Israel, Italy, Netherlands, Norway, Portugal, Romania, Russia, Serbia, Slovenia, Spain, Sweden, Switzerland, Turkey.

The unprecedented disaster of summer 2007, with dozens of dead and millions of burned areas (more than 2.500.000 hectares), put the most tragic end the start of a positive progress. The huge national, environmental and economic damage caused by forest fires have put the issue of forest protection in other bases. The matter now is that the fires regard in particular the survival of entire regions and their sustainable development.

CHAPTER 2

SATELLITE REMOTE SENSING TECHNIQUES FOR FOREST FIRE DETECTION.

2.1 Remote Sensing

Before introducing the rationale at the basis of using satellite data for forest fire detection, a brief description of remote sensing will be provided. Generally, remote sensing refers to the activities of recording/observing/perceiving (sensing) objects or events at far away (remote) places. Namely, the sensors are not in direct contact with the objects or events being observed. The information needs a physical carrier to travel from the objects/events to the sensors through an intervening medium. The electromagnetic radiation is normally used as an information carrier in remote sensing. The output of a remote sensing system is usually an image representing the scene being observed. A further step of image analysis and interpretation is required in order to extract useful information from the image. The human visual system is an example of a remote sensing system in this general sense. In a more restricted sense, remote sensing usually refers to the technology of acquiring information about the Earth's surface (land and ocean) and atmosphere using sensors onboard airborne (aircraft, balloons) or space borne (satellites, space shuttles) platforms.(Figure 2.1)

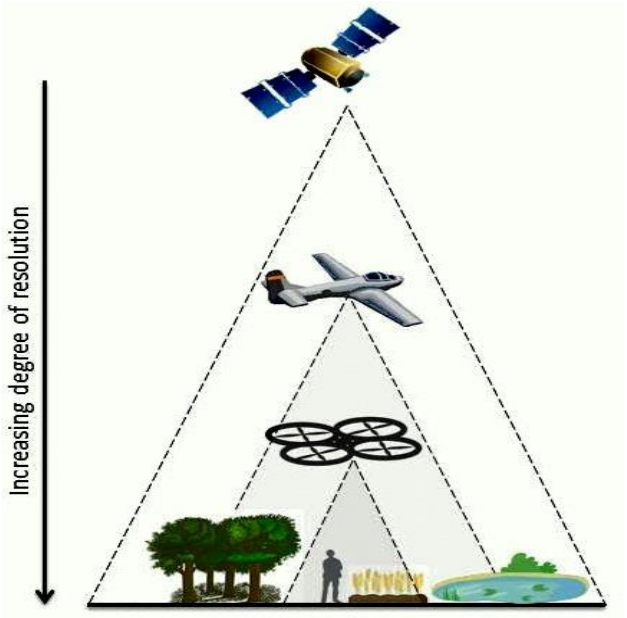

Figure 2.1.Earth observation (Source: https://www.google.as/search?q=Earth+observation&biw)

When looking at the Earth the electromagnetic radiation crosses through the atmosphere. Hence, it is essential to understand the effects that such a layer of atmosphere has on the electromagnetic radiation travelling from the Earth to the sensor. The atmospheric constituents cause wavelength dependent absorption and scattering of radiation. These effects degrade the quality of images. Some of the atmospheric effects can be corrected before the images are subjected to further analysis and interpretation.

A consequence of atmospheric absorption is that certain radiation at specific wavelength in the electromagnetic spectrum are strongly absorbed and effectively blocked. The electromagnetic spectrum is a continuum of energy from shortwave high frequency cosmic waves to longer wavelength low frequency radio waves (Figure 2.2). Our eyes are sensitive to the visible part of the electromagnetic spectrum, a small portion of the whole spectrum.

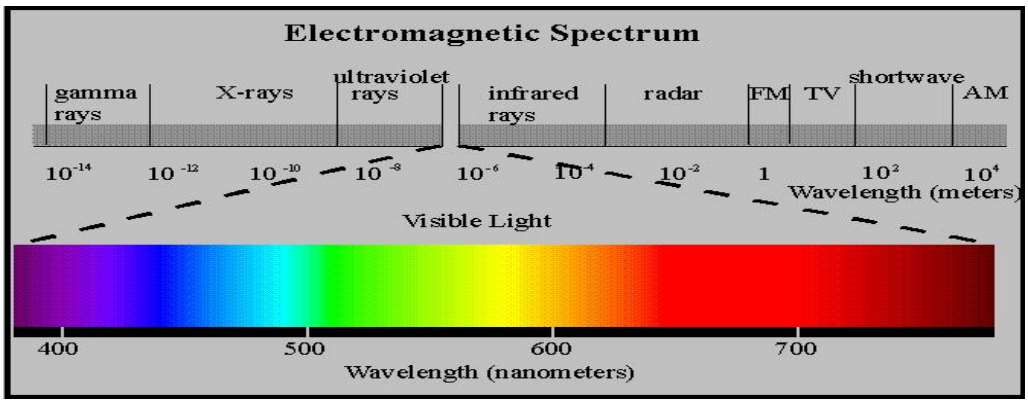

Figure 2.2.Wavelength of Electromagnetic Spectrum. (Source: https://www.google.as/search?q=Earth+observation&biw)

Electromagnetic radiation interacts with matter in different ways across the spectrum. These types of interaction are so different that historically different names have been applied to different parts of the spectrum. Thus, although these "different kinds" of electromagnetic radiation form a quantitatively continuous spectrum of frequencies and wavelengths, the spectrum remains divided for practical reasons in the following sub regions. (Figure 2.3)

1. Ultraviolet radiation
2. Visible radiation
3. Infrared radiation
4. Microwave radiation

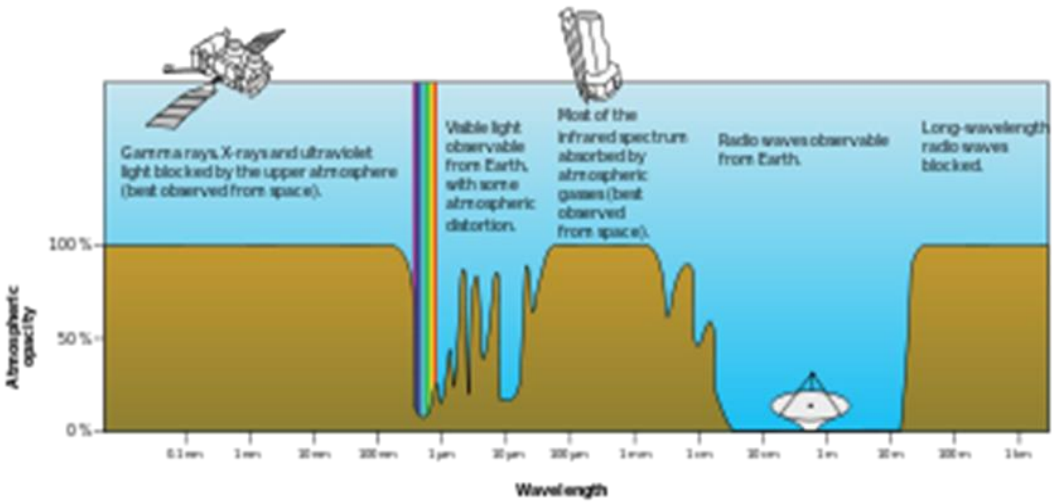

Figure 2.3.Plot of Earth's atmospheric transmittance (or opacity) to various wavelengths of electromagnetic radiation. (Source: https://www.google.as/search?q=Earth+observation&biw)

In the following the main specific characteristics are provided:

Microwaves

The super-high frequency (SHF) and extremely high frequency (EHF) of microwaves are on the short side of radio waves. Microwaves are waves that are typically short enough (measured in millimeters) to employ tubular metal waveguides of reasonable diameter. Low-intensity microwave radiation is used in Wi-Fi, although this is at intensity levels unable to cause thermal heating. Volumetric heating, as used by microwave ovens, transfers energy through the material electromagnetically, not as a thermal heat flux. The benefit of this is a more uniform heating and reduced heating time; microwaves can heat material in less than 1% of the time of conventional heating methods. When active, the average microwave oven is powerful enough to cause interference at close range with poorly shielded electromagnetic fields such as those found in mobile medical devices and poorly made consumer electronics.

Infrared

The infrared part of the electromagnetic spectrum covers the range from roughly 300 GHz to 400 THz (1mm-750 nm). It can be divided into three main parts:

- Far-infrared, from 300 GHz to 30 THz (1 mm - 10 μm). The lower part of this range may also be called microwaves or terahertz waves. This radiation is typically absorbed by so-called rotational modes in gas-phase molecules, by molecular motions in liquids, and by

phonons in solids. The water in Earth's atmosphere absorbs so strongly in this range that it renders the atmosphere in effect opaque. However, there are certain wavelength ranges ("windows") within the opaque range that allow partial transmission.

- Mid-infrared, from 30 to 120 THz (10 - 2.5 μm). Hot objects (black-body radiators) can radiate strongly in this range, and human skin at normal body temperature radiates strongly at the lower end of this region. This radiation is absorbed by molecular vibrations, where the different atoms in a molecule vibrate around their equilibrium positions. This range is sometimes called the fingerprint region, since the mid-infrared absorption spectrum of a compound is very specific for that compound.
- Near-infrared, from 120 to 400 THz (2,500 - 750 nm). Physical processes that are relevant for this range are similar to those for visible light. The highest frequencies in this region can be detected directly by some types of photographic film, and by many types of solid state image sensors for infrared photography and videography.

Visible

Above infrared in frequency comes visible light (400-750nm). The Sun emits its peak power in the visible region, although integrating the entire emission power spectrum through all wavelengths shows that the Sun emits slightly more infrared than visible light. By definition, visible light is the part of the EM spectrum the human eye is the most sensitive to. Visible light (and near-infrared light) is typically absorbed and emitted by electrons in molecules and atoms that move from one energy level to another. This action allows the chemical mechanisms that underlie human vision and plant photosynthesis. The light that excites the human visual system is a very small portion of the electromagnetic spectrum.

Ultraviolet

The wavelength of UV rays is shorter than the violet end of the visible spectrum but longer than the X-ray. The Sun emits significant UV radiation (about 10% of its total power); including extremely short wavelength UV that could potentially destroy most life on land (ocean water would provide some protection for life there). However, most of the Sun's damaging UV wavelengths are absorbed by the atmosphere and ozone layer before they reach the surface. The higher energy (shortest wavelength) ranges of UV (called "vacuum UV") are absorbed by nitrogen and, at longer wavelengths, by simple diatomic oxygen in the air. Most of the UV in the mid-range of energy is blocked by the ozone layer, which absorbs strongly in the important

200–315 nm range, the lower energy part of which is too long for ordinary dioxide in air to absorb. The very lowest energy range of UV between 315 nm and visible light (called UV-A) is not blocked well by the atmosphere, but does not cause sunburn and does less biological damage.

In addition, remote sensing techniques can be classified in two main categories: passive and active (Figure. 2.4). A passive sensor system needs an external energy source. The most important source is the Sun. An active sensor system provides its own energy source. As an example, a radar sensor sends out radio waves and records the reflection waves coming back from the surface. Passive systems are much more common than active systems.Most sensors record information about the Earth's surface by measuring thermal emitting or sun reflected radiation in different portions of the electromagnetic (EM) spectrum. Because the Earth's surface varies in nature, the measured radiation also varies. This variation in energy allows images of the surface to be created. Human eyes see this variation in energy in the visible portion of the EM spectrum. Sensors detect variations in energy in both the visible and non-visible areas of the spectrum.

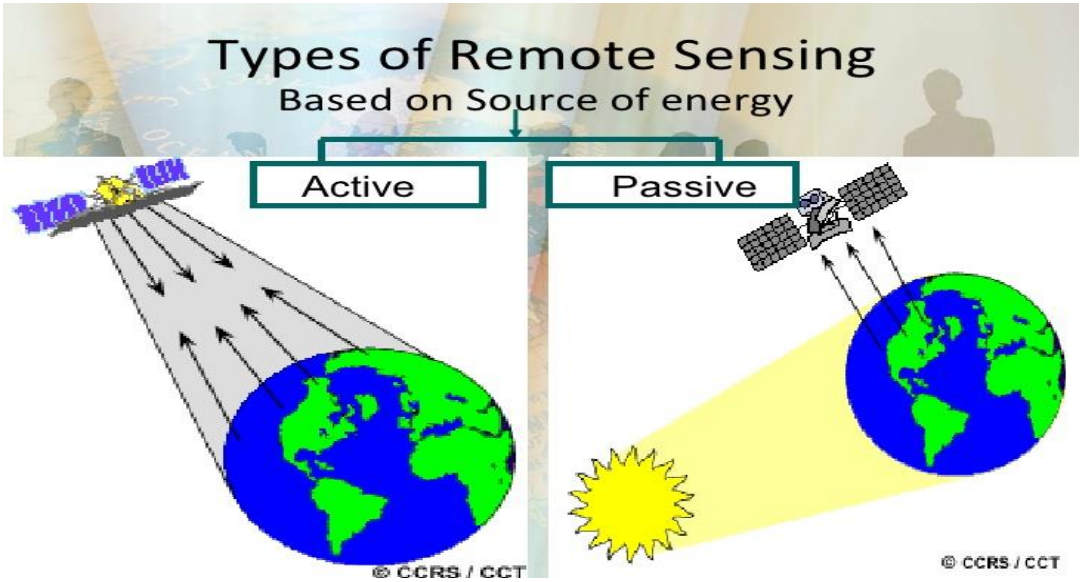

Figure 2.4: Types of remote sensing: Active and Passive (Source: https://www.google.as/search?q=Earth+observation&biw)

2.2 Remote sensing parameters and characteristics

In this paragraph some basics parameters and characteristics of remote sensing will be furnished. One method of classification of Earth observation satellite systems is based on their

orbits. A satellite generally follows elliptical orbit around the Earth. The time taken to complete one revolution of the orbit is called the orbital period. The satellite projection of the orbit on the Earth surface is called satellite ground track.

Remote sensing satellites are often launched into special orbits such that the satellite repeats its ground track after a fixed time interval. This time interval is called the repeat cycle of the satellite. Generally two are the main orbits used: the sun polar and the geostationary orbits. A satellite in a geosynchronous orbit returns to exactly the same place in the sky at exactly the same time of the day. The special case of a geosynchronous orbit that is circular and located in the equator is called geostationary orbit (GEO) (Figure 2.5). A GEO has an orbital eccentricity of zero. A satellite in that orbit, at that chosen distance from Earth in the equatorial plane, moving in a counter-clockwise sense, moves around the Earth exactly with the same speed as the Earth rotates. The satellite then stays fixed in the same place above the Earth in a geostationary orbit. This allows the satellites to observe and collect information continuously over specific areas. From the ground, a geostationary object appears motion less in to the sky. GEO can see whole Earth disk at once due to large distance and also, can see same spot on the surface all the time. It has typically low spatial resolution due to high altitude: e.g. the SEVIRI sensor onboard METEOSAT second Generation (MSG) has a spatial resolution 1 x 1 km in the High Resolution Visible and 3 x 3 km in the other bands. Theses satellites have the best prerequisites for providing information on atmospheric dynamics for short-term forecasting and numerical weather pre-diction (NWP). This is the reason why weather and communications satellites commonly have these types of orbits. With the combination of several GEO meteorological satellites the weather of the whole Earth can be monitored. Satellites in geostationary orbit should be placed in a single ring above the equator. The requirement to space these satellites apart means that there are a limited number of orbital ”slots” available, thus only a limited number of satellites can be placed in geostationary orbit. This hassled to conflict between different countries wishing access to the same orbital slots (countries at the same longitude but differing latitudes). Due to the constant 0 latitude, satellite locations may differ by longitude only.

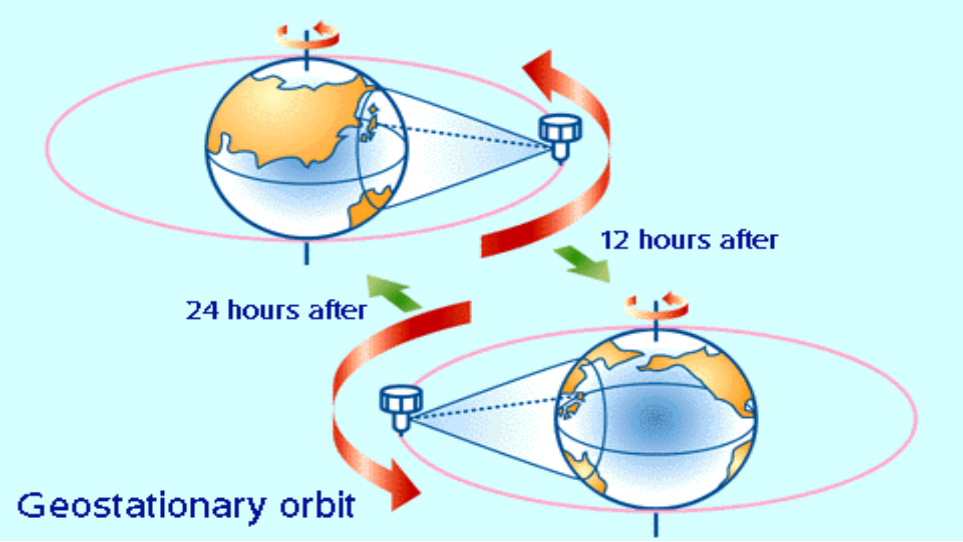

Figure 2.5: Geostationary orbit. (Source: https://www.google.as/search?q=Earth+observation&biw)

On the other hand, polar orbiting satellites (Figure 2.6) overfly higher latitudes even though the satellite does not pass directly over the poles. The altitude of polar orbiting satellites is normally lower than 2000 km. Many remote sensing platforms are designed to follow an orbit (basically north-south) which, in conjunction with the Earth's rotation (west-east), allows them to cover most of the Earth's surface over a certain period of time. These are near polar orbits, so named for their inclination relative to a line running between the North and South poles.

Characteristics of polar and near polar orbits:

- full polar orbit inclined 90 to equator
- typically few degrees off (larger than 90)
- orbital period ,T ,typically 90 to 110 min
- near circular orbit between 300 km and 1000 km (Low Earth Orbit)
- typically higher spatial resolution than geostationary
- rotation of Earth under satellite allows (potentially) total coverage

Many of the LEO near-polar satellite orbits (700 to 1000 km) are also sun-synchronous such that they cover each area of the world at a constant local time of day called local sun time. At any given latitude, the position of the sun in the sky as the satellite passes overhead will be the same within the same season. This ensures consistent illumination conditions when acquiring images in a specific season over successive years, or over a particular area over a series of days. This is an important factor for monitoring changes between images or for mosaic king adjacent images together, as they do not have to be corrected for different illumination conditions.The mechanism for providing this precession of the orbit is achieved using the effects of the non-uniformity of the Earth gravitational field that arises from the fact that the Earth is not a perfect sphere.

The rate of change for the orbital node (precession rate -dΩ/dt) is approximately given by:

$$\frac{d\Omega}{dt} = -\frac{3}{2} J_2 R^3 \sqrt{9} \frac{\cos I}{R^{7/2}}$$

- Here J2= 0.00108 which is the second harmonic of the Earth geopotential and I the inclination angle.
- precession rate = function of I and r
- For I= 98, precession period is 1 year! I.e., the position of the orbit relative to the sun is constant ⇒satellite passes over same latitude at the same local time ⇒useful to avoid varying illumination conditions caused by different time of day⇒used by most remote-sensing satellites
- Note: seasonal variation of illumination cannot be avoided!
- ground track of sun-synchronous, near polar orbiting satellite: wavy line

After a number of orbits, sub-satellite point retraces its path. In near-polar orbits, areas at high latitudes will be sensed more frequently than the equatorial zone due to the increasing overlap in adjacent swaths as the orbit paths come closer together near the poles. If the orbit is also sun synchronous, the ascending pass is most likely on the shadowed side of the Earth while the descending pass is on the sunlit side. Sensors recording reflected solar energy only image the surface on a descending pass, when solar illumination is available. Active sensors which provide their own illumination or passive sensors that record emitted radiation can also image the surface on ascending (02 night time) pones.

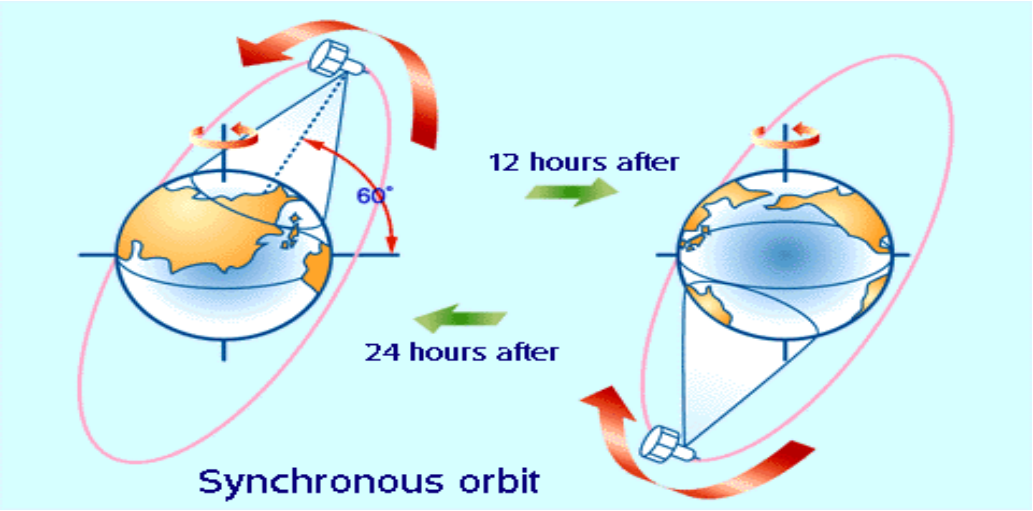

Figure 2.6: Synchronous orbit. (Source: https://www.google.as/search?q=Earth+observation&biw)

Moreover, early remote sensing devices recorded photographic images on film (taken by cameras) or traces printed onto paper rolls (sonar devices). Both routes created an image in

analogue format. These images were fixed and could not be subject to very much manipulation (correction, change of contrast or color etc.). More recently, they started to be converted into an electronic digital format for limited manipulation. Most modern sensors now record their information in digital format, often as digital images. A digital image is made up of numbers, which represent image attributes such as brightness, color or radiance at different wavelengths, and position location for each point or picture element in the image. The smallest sized picture element on an image is called a pixel. A digital image, commonly known as a raster image, is made up of pixels arranged in rows and columns. The resolution cell dimensions corresponding to each of these pixels give the spatial resolution of the image. Remote sensors measure differences and variations of the electromagnetic radiation of resolutions (spatial, temporal, spectral, and radiometric) each of which characterize the accuracy and usefulness of remote sensors to habitat mapping.

The **Spatial resolution** is a measure of the fineness of spatial detail of an image. For digital images, this refers to the diameter of the ground resolution cell corresponding to a single pixel, (Figure 2.6).

Satellite data on the basis of their spatial resolution are classified as:

- Very high spatial resolution (0.6-4m)
- High spatial resolution (4-30 m)
- Medium spatial resolution (50-250 m)
- Low spatial resolution (250 > 1000m).

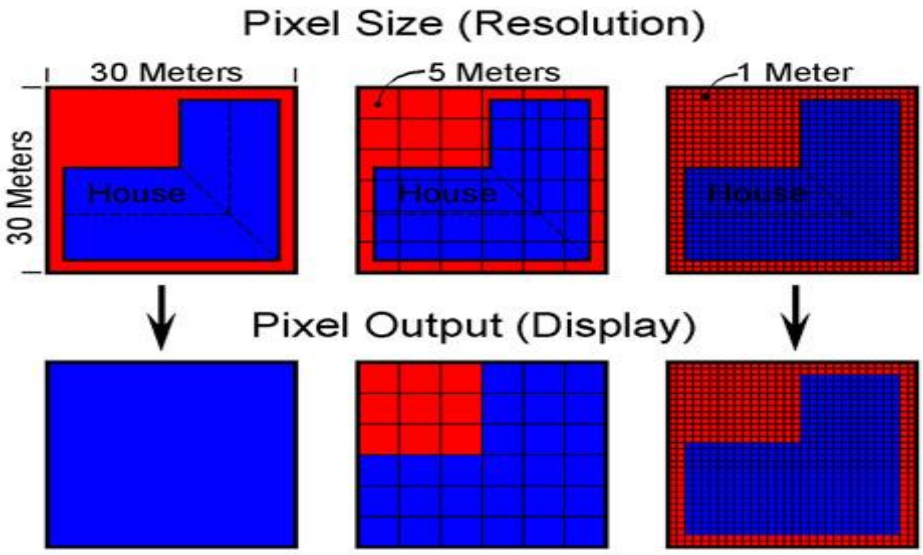

Figure 2.6: Spatial resolution (Source: https://www.google.as/search?q=Earth+observation&biw)

The Spectral **resolution** is defined through the number of spectral bands and their width. Their purpose is to capture the differences in the reflection characteristics of different surfaces. While the human eye only recognizes the visible spectrum of light, a satellite sensor can, depending on the type, measure radiation in many spectral different. The majority of passive Earth observation satellites have between three and eight bands of regions called multispectral. Hyper spectral sensors have more than 100 bands, several thousands of bands on typical of interferometry sensors (ultra spectral).

The **temporal resolution** is given as the time interval between two measurements performed on the same area by a satellite sensor it is also called repetition rate and is determined by the altitude and orbit of the satellite as well as by its sensor characteristics (viewing angle).The temporal resolution is reduced by clouds which present selected visible or emitted infrared radiation, that does not penetrate through clouds, to reach the sensor. Areas of the Earth covered by clouds cannot be properly depicted when a satellite passes over them.

Satellite data on the basis of their temporal resolution are classified as:

- High temporal resolution: < 24 hours - 3 days
- Medium temporal resolution: 4 - 16 days
- Low temporal resolution: > 16 days

Finally, the sensitivity of a sensor to brightness values is known as its radiometric resolution. This metric is usually articulated in terms of binary bit-depth, which refers to number of grayscale levels at which data are recorded by a particular sensor (Jensen 2005). The binary bit-depth is typically expressed in the following ranges of grayscale levels: 8-bit (0–255), 10-bit (0–1,023), 11-bit (0–2,047), 12-bit (0–4,095) and 16-bit (0–65,535) (Figure 2.8).The finer or the higher the radiometric resolution is, the better small differences in reflected or emitted radiation can be measured, and the larger the volume of measured data will be.

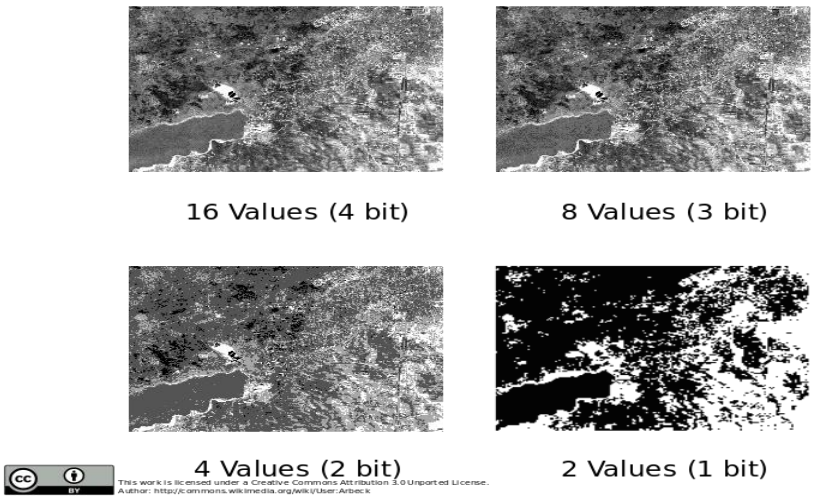

Figure 2.8: Grayscale levels.

2.3 Fire forest detection using remote sensing.

Before addressing the features of each sensor that are suitable for fire detection, is to thoroughly understand the physic principle of fire detection. The detection of hot spots is based on measurement, performed in the middle and infrared spectral sensor. The law of Plank's, Wien's, and Stefan-Boltzmann's govern the detection process. A fire can be detected by the in frond channels in the spectral regions 11-12μm and 3-4 μm. For example, a body with a temperature of 300 K (Earth's means temperature) will have its maximum emitance close to 10 μm. The radiation emitted by a body with temperature of 800 K, will have maximum emittance close to 3.6 μm (Figure 2.9). In the graph, there is a perceptible difference when the temperature is 300K and when is 500K between MIR and TIR. In the first case the radiance received in MIR is lower than the one received in TIR, while in the second case the radiance is higher in MIR.

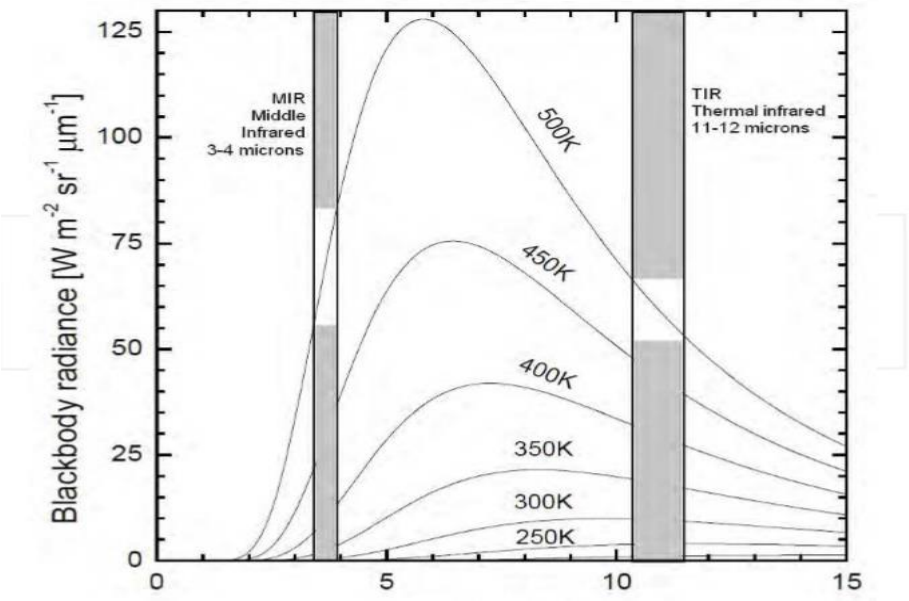

Figure 2.9: Law of Planck, showing blackbody emission for MIR and TIR (Source: Abel Calle, José Luis Casanova (2012))

The main problem is the false alarms that in the 4μ range and cannot obtain positive fire detection. Specifically (Abel Calle, José Luis Casanova (2012)), a high radiance signal does not necessarily correspond to a high temperature pixel, except in the case of night observation, when the reflection component, evidently, does not exist. As is to be expected, the radiance that gets to the sensor operates in that part of the spectrum where, as is the 4 μm case the reflection and the emission effects superimpose. The value of the reflected component $L_{reflection}$ is $\frac{\alpha E_0 \cos(\theta sun)}{\pi}$, with θ_{sun} being the sun's zenith angle, E_0 the extraterrestrial sun's irradiance in that spectral band and α the spectral reflectance (the atmospheric effect are not included). The emission component, $L_{emission}$ is

(1-α)*B (λ, $T_{surface}$), in which B (λ, T) is the function of Planck, λ the wavelength in that spectral band and $T_{surface}$ the surface temperature observed by the sensor. Note that, for not transmitting bodies is ε= (1-α) and α= (1-ε) with ε emissivity. If a surface has a high value of reflectance in the MIR region, radiance coming from source is high and brightness temperature will be higher than surface temperature by several Kelvin. As an example, it can be observed that for a reflectance value of 20% and a sun's zenith angle of 30º the brightness temperature can increase more than 20 K higher due to reflectance effect.When the contribution of the reflection component is very marked and as a consequence the radiance increases in the middle infrared band, a pixel appears with an apparent high temperature that can be mistaken with a hot spot, producing a false alarm. These situations are more frequent in the highest spatial resolution sensors and when high reflectance surfaces coincide with sun satellite geometrical situations close to specular reflection conditions. This is the case of small water surfaces, for example, and it is called sun glint. It must be pointed out that the problem of the appearance of false alarms is more difficult to solve than the detection itself due to the difficulty in separating both effects. Finally, it must be mentioned that clouds are also an important source of false alarms due to the sun's reflection. Their reflectance is high and they cause a strong signal in the MIR spectral band in situations of very high sun zenith angles.

As we mentioned in the previous chapters forest fires represents serious problems not only from a natural point of view, but also for the society and the economy. Mainly for this reason fires should be detected as soon as possible. A number of techniques can be used for fire detection, but the ones based on satellites data present several advantages in terms of operational and economical perspectives. Thanks to the satellite synoptic view, they can be used to monitor very large areas, with relatively low cost, high scene updating frequency which is critical for real-time fire monitoring.

Currently, for early warning systems the satellites that can be useful are the polar orbiting, such us, AVHRR, MODIS, ASTER and Lansat as well as geostationary satellites such us MSG, GOES and MTSAT-IR. The polar orbiting satellites having temporal resolution up to 1-3 days and spatial resolution up to hundreds of meters cannot detect short duration fires but may be useful in identifying small fires. On the other hand, GEO satellites having higher temporal resolution (up to 15 minutes) can give information about phenomena which change continuously, hence they are very useful to map active fire even if with possible limitations concerning fire size. The AVHRR was used for remotely monitoring cloud cover and Earth surface temperature. Note that with the term surface can be included the surface of the Earth, as well as the upper surfaces of clouds. AVHRR uses 6 detectors to collect different bands with a swath of about 2400 Km, a spatial resolution of

1.1km at sub-satellite pixel and a temporal resolution of about 12 hours. It transmits 5 data channels at a time, since channel 3A (1.6 μm) operates just Day time and 3B channel (3.9μm) just Night time cannot operate at the same time (http://noaasis.noaa.gov/NOAASIS/ml/avhrr.). Several studies (Malingreau, 1990; Prins and Menzel, 1994) have shown that fire occurrence and spread tend to be greatest near solar noon (Figure 2.10) when winds and low relative humidity favor fire spread.

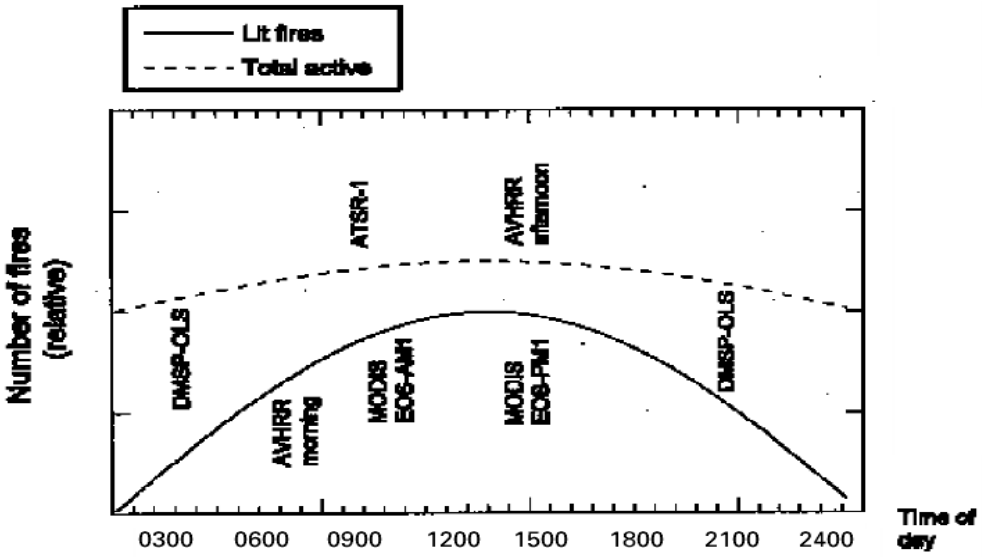

Figure 2.10: Schematic diagram of orbital platforms that provide broad-area coverage. (Source: http://sinae.gub.uy)

ASTER (Advanced Space borne Thermal Emission and Reflection Radiometer) imagery is available since 2000 from the NASA Terra satellite. It provides high-resolution images of the Earth in 14 different bands of the electromagnetic spectrum, ranging from visible to thermal infrared. The resolution of images ranges between 15 and 90 meters and **c**onsists of three separate instrument subsystems: the VNIR (Visible near Infrared), a backward looking telescope which is only used to acquire a stereo pair image, the SWIR (Short Wave Infrared), a single fixed aspheric refracting telescope failed on 2008 and TIR (Thermal Infrared) sensor. ASTER data are used to create detailed maps of land surface temperature, emissivity, reflectance, and elevation. Moderate Resolution Imaging Spectroradiometer (MODIS), flights onboard Terra (since 2000) and Aqua satellites (since 2002), recording 2 images at day and 2 images at night. MODIS has a swath width of 2330 km cross track and 10km along track which leads to a maximum scan angle of 55^{o} at both ends of the flight line. Therefore, the instantaneous field of view increases from 1x1 km at nadir to about 2x5 km at the maximum scan angle (Susan Philip-thesis). The solar zenith angle and the scan angle are two very important influences on the thermal anomaly detected by a sensor. Considering all other conditions constant, a fire would be prominent as compared to its background at larger solar zenith

angles than at the smaller ones. At smaller solar zenith angles the influence of solar radiation is very high and therefore the 3.9 temperature is raised. With increasing scan angle the pixel area increases and therefore the apparent brightness temperature decreases for the pixels. Comparing this effect for 3.9 μm and 10.8 μm it is seen that the temperature decrease is much more for 3.9 μm. The decrease is mainly noticed for small fires (<100 ha) however in case of large fires (>100 ha) the temperature of 3.9 μm remains the same and that of 10.8 decreases. An additional cause for the decrease in brightness temperature due to scan angle increase is the increase in atmospheric absorption (GIGLIO.; et al., 1999). One more polar orbiting satellite is LandSat. The original missions (1970s – early 1980s) used the Multispectral Scanner (MSS) which was only capable of detecting scars. Current Landsat series satellites use the Thematic Mapper (TM) and Enhanced Thematic Mapper Plus (ETM+) to provide land surface information. The high spatial resolution Landsat Thematic Mapper (TM), (1993,Justice, Malingreau, Setzer, Satellite, Dahlem), includes a SWIR infrared channel (2.08-2.35 ~m) with a 30 m spatial resolution, which permits active fires to be detected. A 700 K fire that occupies 20% of the 30 m pixel will saturate such a channel.

Continuing with GEO satellites, one of them is Meteosat Second Generation (MSG). It has been established (Susan Philip-thesis) under a cooperation between the European space Agency (ESA) and the European Organization for the Exploitation of Meteorological Satellites (EUMETSAT). The MSG is a spin-stabilized satellite with a repeat cycle of 15 minutes which gives unprecedented multispectral observation of rapidly changing environment (Schmetz et al. 2002). The most important instrument on MSG is the Spinning Enhanced Visible and Infrared Imager (SEVIRI). The SEVIRI images the Earth in a wide spectral range with 12 channels, at an interval of 15 minutes. For channels 1-11, a full disk image consists of 3712 * 3712 pixels, however for the HRV channel a complete image consists of 11 136 * 5568 pixels and it covers only half-disk in an East-West direction. One more GEO satellite is the Geostationary Operational Environmental Satellite system (GOES), operated by the United National Environmental Satellite, Data and information Service (NESDIS). The GOES satellite has a lot of generations, such as, SMS-1^{+}, SMS-2^{+}, GOES-1, GOES-2, GOES-3, GOES-4,GOES-5, GOES-6, GOES-7, GOES-8, GOES-9, GOES-9*, GOES-10, GOES-11, GOES-12, GOES-13, GOES-14$^{\wedge}$, GOES-15, GOES-R. The position of satellites is 35.800 km (22.300 miles) above the Earth, allowing the satellites full-disc view of the Earth. It must be emphasized, that the next generation GOES-R of National Oceanic and Atmospheric Administration (NOAA), is appropriate for monitor hazards, such as, aerosols, dust, storms, volcanic, eruptions, forest fires, etc. Among its six primary instruments, the Advanced Baselines Imager (ABI), a sixteen channel imager with two visible channels and four near infrared channels, will provide (4x) improved resolution, (5x) faster coverage, and more coverage

simultaneously. With the Geostationary Lighting Mapper has continuous coverage of total lighting flash rate over land and water and increased dynamic range, resolution and sensitivity in monitoring solar X-ray flux with the solar Ultraviolet Imager (SUVI). Similar to GOES, in terms of spectral coverage, is the MTSAI-1R JAMI a multi-functional three-axis stabilizes satellite that is being produced by the Japan. The JAMI includes one visible band (0.72μm) and 4 infrared bands (3.75, 6.75, 10.8, and 12.0 μm). The current JAMI design specifies a spatial resolution at nadir of 0.5 km in the visible and 2km in the IR bands with the 12-bit quantization, although the data may be disseminated to the user community with the reduced resolution of 1km in the visible and 4km in the IR. The increased spatial resolution of the MTSAI JAMI, spectral differences, and the low saturation temperature will require modifications to the current methodology used to identify and characterize fires with the GOES. The JAMI will offer a unique opportunity to provide early warning in the detection of smaller fires which are not detectable by other geostationary platforms. Minimum detectable fire size estimates suggest that the spectral configuration and 2km spatial resolution of 3.75μm band on MTSAI-1R will allow it to detect significantly smaller fires than with the GOES Imager. With the proposed specifications, the MTSAI-1R will be able to detect a 0.03 ha fire burning at 750K at the equator. The minimum detectable fire size at 50^{o} N is 0.06 ha. This is 5 times smaller than the GOES minimum detectable fire size (Global Geostationary Fire Monitoring System, Elaine M. Prins, Donna McNamara, Christopher C. Schmidt).

CHAPTER 3

THE ROBUST SATELLITE TECHNIQUES (RST) AND MOD14 ALGORYTMS APPROACHES FOR FIRE FOREST DETECTION.

3.1 MODIS sensor

The two algorithms used in this thesis for fire detection use MODIS data, its main characteristics will be briefly described in the following (see also Table 3.1). MODIS with 36 bands developed for the Advanced Very High Resolution Radiometer (AVHRR) and Visible and Infrared Scanner (VIRS) (Giglio, Kendall & Justice, 1999; Giglio, Kendall, & Mack, in press) and experience with the first 2 years of high quality MODIS data (Giglio, Descloitres, Justice, Kaufman; 2003).

MODIS acquires data from an orbit 705 kilometers above the Earth. To complete one orbit around it takes about 98 minutes, which makes it well suited for gathering data about moderately fast-dynamic events like forest fires. In addition, considering that is onboard both of Aqua and Terra, it can also detect if present differences in fires between diurnal and nighttime conditions. This frequent coverage is especially important during fire seasons, when huge fires can start in the blink of an eye. Having diurnal and nighttime view of the same area allows also scientists to monitor over time changes in fire frequency, intensity or location.

The MODIS algorithm uses brightness temperatures derived from the 4 μm (21 and 22 channels, both of which are used by the detection algorithm) and 11 μm (channel 31) channels, denoted by T_4 and T_{11}, respectively. Channel 21 saturates at nearly 500K and channel 22 saturates at 331K. Since the low saturation channel 22 is less noisy and has smaller quantization error, it is replaced with the high saturation channel (e.g., 21) to derive T_4 when this channel (e.g., 22) saturates or has missing data. T_{11} is computed from the 11 μm channel, which saturates at 400K for the Terra MODIS and 340K for Aqua MODIS. Apart of this, the 12μm channel (channel 32) is used for cloud masking and the brightness temperature for this channel is denoted by T_{12}. However the 250 m resolution red and near infrared channels, aggregated to 1 km, are used to reject false alarms and mask clouds. The 500 m 2.1 μm band, also aggregated to 1 km, is used to reject water pixels to

avoid false alarms (Giglio, Descloitres, Justice, Kaufman; 2003). In Table 3.2 the MODIS channels at the basis of MOD-14 algorithm are indicated.

Primary Use	Band	Bandwidth	Spectral Radiance
Land/Cloud/Aerosols Boundaries	1	620-670 nm	21.8 W
	2	841-876 nm	24.7 W
Land/Cloud/Aerosols Properties	3	459-479 nm	35.3 W
	4	545-565 nm	29.0 W
	5	1230-1250 nm	5.4 W
	6	1628-1652 nm	7.3 W
	7	2105-2155 nm	1.0 W
Ocean Color Phytoplankton Biogeochemistry	8	405-420 nm	44.9 W
	9	438-448 nm	41.9 W
	10	483-493 nm	32.1 W
	11	526-536 nm	27.9 W
	12	546-556 nm	21.0 W
	13	662-672 nm	9.5 W
	14	673-683 nm	8.7 W
	15	743-753 nm	10.2 W
	16	862-877 nm	6.2 W
Atmospheric Water Vapor	17	890-920 nm	10.0 W
	18	931-941 nm	3.6 W
	19	915-965 nm	15.0 W

Surface/Cloud Temperature	20	3.660-3.840 μm	0.45 W (300 K)[1]
	21	3.929-3.989 μm	2.38 W (335 K)[1]
	22	3.929-3.989 μm	0.67 W (300 K)[1]
	23	4.020-4.080 μm	0.79 W (300 K)[1]
Atmospheric Temperature	24	4.433-4.498 μm	0.17 W (250 K)[1]
	25	4.482-4.549 μm	0.59 W (275 K)[1]
Cirrus Clouds Water Vapor	26	1.360-1.390 μm	6.0 W
	27	6.535-6.895 μm	1.16 W (240 K)[1]
	28	7.175-7.475 μm	2.18 W (250 K)[1]
Cloud Properties	29	8.400-8.700 μm	9.58 W (300 K)[1]
Ozone	30	9.580-9.880 μm	3.69 W (250 K)[1]
Surface/Cloud Temperature	31	10.780-11.280 μm	9.55 W (300 K)[1]
	32	11.770-12.270 μm	8.94 W (300 K)[1]
Cloud Top Attitude	33	13.185-13.485 μm	4.52 W (260 K)[1]
	34	13.485-13.785 μm	3.76 W (250 K)[1]
	35	13.785-14.085 μm	3.11 W (240 K)[1]
	36	14.085-14.385 μm	2.08 W (220 K)[1]

Table 3.1: 36 spectral bands of MODIS (Source: http://modis.gsfc.nasa.gov/about/specifications.php)

Primary Use	Band	Bandwidth	Spectral Radiance
Land/Cloud/Aerosols Boundaries	1	620-670 nm	21.8 W
	2	841-876 nm	24.7 W
Land/Cloud/Aerosols Properties	7	2105-2155 nm	1.0 W
Surface/Cloud Temperature	21	3.929-3.989 μm	2.38 W (335 K)[1]
	22	3.929-3.989 μm	0.67 W (300 K)[1]

Surface/Cloud Temperature	31	10.780-11.280 μm	9.55 W (300 K)[1]
	32	11.770-12.270 μm	8.94 W (300 K)[1]

Table 3.2: MODIS channels used in MOD14 detection algorithm

Furthermore, the algorithm assigns each pixel of the MODIS swath to some classes like missing data, cloud, water, non-fire, fire, or unknown. Cloud and water pixels are identified using an internal cloud mask and the water mask within the MODIS Level 1A geolocation products (MOD13 and MYD03), and are respectively assigned to the classes cloud and water. The processing continues on the remaining clear land pixels.

As i mentioned to previous chapter, for the identification of fire pixels there are two logical paths, a simple absolute threshold test and a series of contextual tests designed to identify the majority of active fire pixels that are less obvious. The fixed threshold must be set sufficiently high so that it is triggered only by very unambiguous fire pixels (T_4>360 K (320K at night)) (Giglio, Descloitres, Justice, Kaufman; 2003). For implementing the contextual test, a background characterization should be carried out. That means that valid neighboring pixels in a window centered on the potential fire pixel are identified and are used to estimate a background value. The window starts (Giglio, Descloitres, Justice, Kaufman; 2003) as a 3 × 3 pixel square box around the potential fire pixel. Due to the triangular along-scan response of the MODIS instrument (Kaufman et al., 1998b), the two along scan pixels adjacent to the potential fire pixel are deemed unreliable and excluded from the background characterization. The box is increased to a maximum of 21 × 21 pixels, as necessary, until at least 25% of the pixels within the window have been deemed valid, and the number of valid pixels is at least eight. During this step, an optimized nearest-neighbor search is used to correct for the "bowtie" effect, or overlap between MODIS scans (Nishihama et al., 1997). These look for the characteristic signature of an active fire in which both 4 μm brightness temperature and the 4 and 11 μm brightness temperature differences depart substantially from that of the non-fire background. Additional tests were used, to avoid false alarms caused by sun glint, desert boundaries and coastal mixed pixels. Unlike most contextual fire detection algorithms designed for satellite sensors that were never intended for fire monitoring (e.g. AVHRR, VIRS, ATSR), there is no upper limit to the largest and/or hottest fire that can be detected with MODIS. (Figure 3.1)

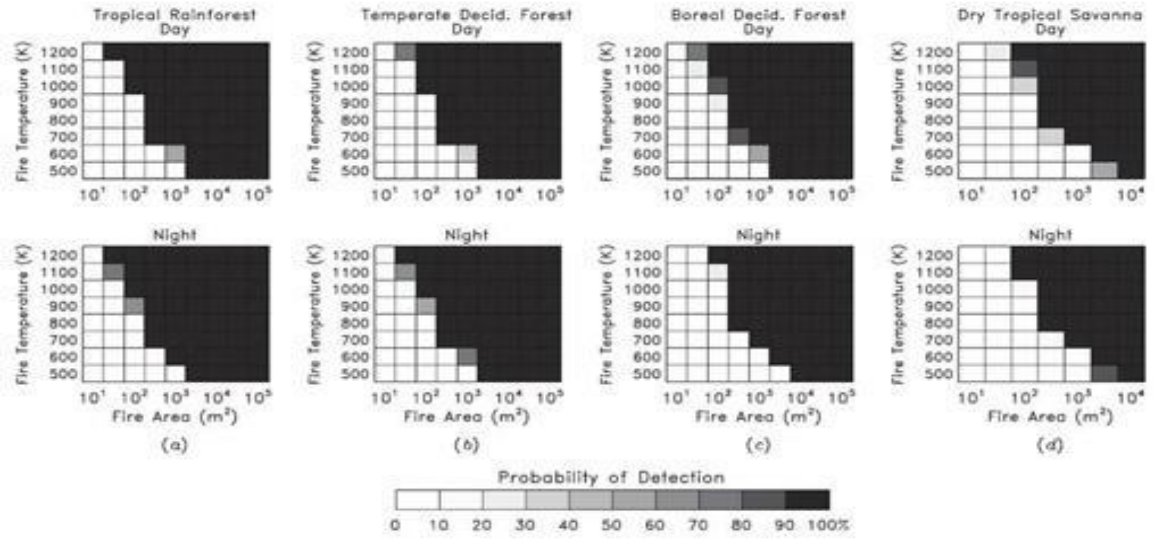

Figure 3.1: Day and night relationship of fire size and fire temperature, in different biomes, to the probability of being detected by MODIS (Source: https://www.google.com.pg/search?q=Day+and+night+relationship+of+fire+size+and+fire+temperature&biw=1440&bih)

3.2 The Robust Satellite Techniques (RST) approach for fire forest.

The methodology used in this work is based on the Robust Satellite Techniques for forest fire detection and monitoring (RST-FIRES- Marchese, Corrado, Filizzola, Mazzeo, Paciello, Pergola, Tramutoli, et al; 2010)

The RST approach (e.g. Tramutoli, 1998; 2007), is a multi-temporal scheme of data analysis already successfully used to study for several natural and environmental hazards (e.g. volcanic activity in Pergola 2004a, b; Pergola et al., 2004; seismically active areas in Aliano et al., 2008; Corrado et al., 2005; Filizzola et al., 2004; Genzano et al., 2009; hydrological risk in Lacava et al., 2005; oil spill in Casciello et al. 2007). This algorithm is based on the analysis of multi-year historical series, of homogeneous satellite records (i.e. collect in the same month of year, at same hour of the day), for the identification of signal normal behavior at pixel level. These values are usually given in terms of time average and standard deviation (Mazzeo, Marchese, Filizzola, Pergola, Tramutoli, et al; 2007). Three main steps are at the basis of the RST implementation.

Pre-processing is the first one, and concerns with the construction of the historical data-set of homogeneous (same platform, period of the day, period of the year, etc.) satellite data. These data should show accuracy in terms of navigation and co-location of all imagery not lower than the typical spatial dynamic of the phenomena of interest. Furthermore, in this step some masks are created (cloud-mask, events-mask, discarding-mask), to avoid to include in the data set known spurious measurements and/or outlines.

The computation of reference fields is the second step and the third change detection step it deals with the computation of a local variation index, named ALICE (Absolutely Llocal index of Change of Environment), that estimates at pixel level how much the satellite signal at time t deviates from its normal behavior.

$$\otimes_{\mathrm{V}}(\mathrm{x},\mathrm{y},\mathrm{t}) = \frac{[V(x,y,t)-\mu_V(x,y)]}{\sigma_{\mathrm{V}}(\mathrm{x},\mathrm{y})} \quad (1)$$

Where V(x, y, t) is the satellite signal measured at time t in a specific spectral band (or in a combination of more spectral bands) at location (x, y), while $\mu_V(x,y)$ represent the temporal mean and $\sigma_{\mathrm{V}}(\mathrm{x},\mathrm{y})$ the standard deviation of the same signal V(x, y) at the same location (x, y), calculated using multi-year historical series of homogeneous cloud free satellite records. Mainly, an anomaly of RST is detected (RST-FIRES, Filizzola, Corrado, Marchese, Mazzeo, Paciello, Pergola, Tramutoli) when the signal V(x, y, t) is greater than the expected value μ_{V}(x, y) and σ_{V} (x, y), at the same time the signal excess is significantly greater than the signal normal fluctuations.

RST-FIRES, first test are based on the satellite signal acquired in the MIR spectral band (the most suitable to identify high temperature surfaces). The index reported in equation (1) is then expressed as:

$$\otimes_{\mathrm{MIR}}(\mathrm{x},\mathrm{y},\mathrm{t}) = \frac{[T_{MIR}(x,y,t)-\mu_{MIR}(x,y)]}{\sigma_{\mathrm{MIR}}(\mathrm{x},\mathrm{y})} \quad (2)$$

Equation (2) reports the simplest index which RST-FIRES is based on. Where $T_{MIR}(x,y,t)$ is the brightness temperature measured in the MIR channels, at (x, y) location at time t, and $\mu_{MIR}(x,y)$ and $\sigma_{\mathrm{MIR}}(\mathrm{x},\mathrm{y})$ have the same meaning as before.

It should be stressed that before the calculation of the above index the OCA cloud detection scheme (Pietrapertosa et al., 2000, Cuomo et al., 2004) is implemented, in order to remove cloudy pixels from the satellite scenes. Being RST-FIRES tunable, various level of the $\otimes_{\mathrm{MIR}}(\mathrm{x},\mathrm{y},\mathrm{t})$ index may be used in order to discriminate forest fires having different relative intensity (i.e. high positive values of the MIR index may be related to the presence of fires with large/high relative intensity. Similarly, lower MIR index values may refer to events with a lower size and/or relative intensity because of different burned fuel, or different extension within the pixel area. Site effects, typically occurring at the same places under the same observational conditions (same period of the year and same hours of the day), which may affect fixed threshold methods, does not influence RST-FIRE reliability. They are considered in fact, as normal event determining low values of the $\otimes_{\mathrm{MIR}}(\mathrm{x},\mathrm{y},\mathrm{t})$ index even in present of quite high $\mathrm{T}_{\mathrm{MIR}}$ (x, y, t) values. It is worth mentioning that analyzing signal in the sole MIR spectral band, false positives related to atmospheric effects, which affect reliability of multi-channel and contextual algorithms, are not generated.

To overcome a residual problem due by some weather/climatic factors, which can produce a local increase of the measured TB, another RST-based index is then applied:

$$\otimes_{\mathrm{MIR-TIR}}(\mathrm{x,y,t}) = \frac{[\Delta \mathrm{T}(x,y,t) - \mu_{\Delta \mathrm{T}}(x,y)]}{\sigma_{\Delta \mathrm{T}}(\mathrm{x,y})} \quad (3)$$

Where $\Delta T(x, y, t) = T_{MIR}(x, y, t) - T_{TIR}(x, y, t)$, is the difference between brightness temperatures measured at location (x, y) in MIR (T_{MIR}) and the signal measured in the Thermal Infrared band (TIR) at around 11 μm wavelength. While $\mu_{\Delta T}(x, y)$ and $\sigma_{\Delta T}(x, y)$ are the corresponding temporal mean and standard deviation computed (using all available historical images) on the basis of the values of the cloud-free brightness temperatures (at the same pixel (x, y), at the same time and the same month of the year.). The combination of the above-mentioned indices increasing the trade-off between reliability and sensitivity guarantees a more effective identification of hot spots.

The use of a two-channel (RST-FIRES, Filizzola, Corrado, Marchese, Mazzeo, Paciello, Pergola, Tramutoli, 2007) index allows us to better emphasize the presence of fires that occupy a very small portion of a satellite pixel since the hottest portion of a pixel gives a greater contribution to the full pixel radiance in shorter wavelengths (MIR) than in longer wavelengths (TIR) (Dozier, 1981).

In conclusion, as mentioned before RST based just on satellite data it is quite straightforward (RST-FIRES, Filizzola, Corrado, Marchese, Mazzeo, Paciello, Pergola, Tramutoli, 2007) to export RST-FIRES to different areas/conditions/fire regimes and different sensors onboard polar and geostationary platforms.

3.3 MOD14/MYD14 algorithm for fire detection.

The other algorithm whose results have been analyzed in this thesis is the standard NASA MOD/MYD14 one. The outputs of this algorithm are daily provided by NASA as a Level 2 product. The collection 6 of such a product has been just released taking the place of collection 5, which has been provided since mid-2006.

The MODIS divided in some products, such as Level 0, Level 1, and Level 2, Level 2G, Level 3 and Level 4. The Level 2G, Level 3 and Level 4 products were the most important for the analysis, are defined on o global 250 m (172800 x 86400 pixels), 500m or 1km (43200 x 21600 pixels), sinusoidal grid and they are divides into fixed approximately 10^0 x 10^0 in size. Each tile (Giglio, 18 February 2010) is assigned a horizontal (H) and vertical (V) coordinate, ranging from 0 to 35 and 0 to 17, respectively (Figure 3.2). The tile in the upper left (i.e. northern most and western most) corner is numbered (0, 0).

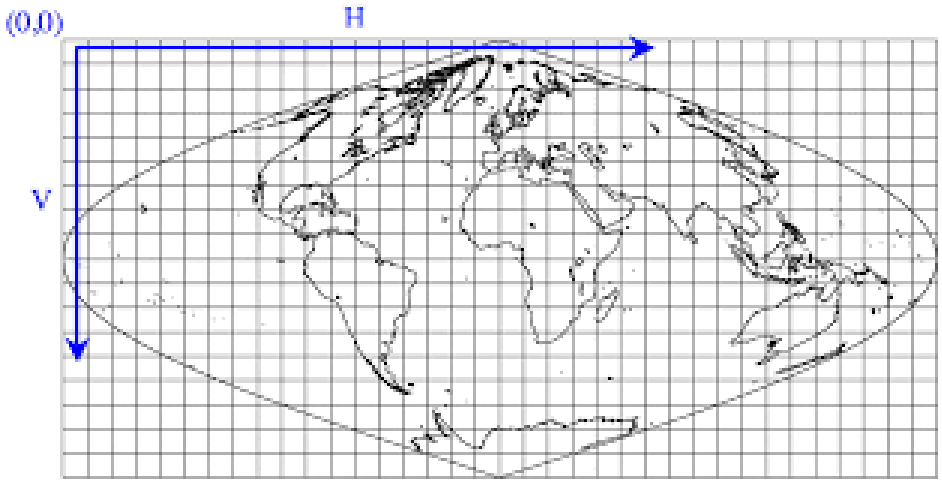

Figure 3.2: MODIS tiling scheme. (Source: https://www.google.com.pg/search?q=MODIS+tiling+scheme.&biw=1440&bih)

The MOD14 level 2 product contains (Giglio, 18 February 2010) an active fire mask (Table 3.3) that flags fires and other relevant pixels (e.g. cloud), a pixel-level QA image that includes 19 bits of QA information about each pixel and a fire pixel table which provides 16 separate pieces of radiometric and internal-algorithm information about each fire pixel detected within a granule. Also contains extensive mandatory and product-specific metadata that includes the number of cloudy, water, non- fire, fire, unknown and other type, pixels (Table 3.4). After level 2 is the level 2G which is a Daytime and Nighttime fire product, with binned data without resembling. Moreover (Justice, Giglio, Korontzi, Owens, Morisette, Roy, Descloitres, Alleaume, Petitcolin, Kaufman, 2002) the Level 2G format provides a convenient geocoded data structure for storing granules and enables flexibility for subsequent temporal compositing and data projection.

Class	Meaning
0	not processed (missing input data)
2	not processed(other reason)
3	Water
4	Cloud
5	non- fire clear land
6	Unknown
7	low-confidence fire
8	nominal-confidence fire

9	high-confidence fire

Table 3.3: MOD14/MYD14 fire mask pixel classes. (Source: Giglio, 18 February 2010)

Attribute Name	**Description**
Fire Pix	Number of fire pixels detected in granule.
Missing Pix	Number of pixels in granule lacking valid data for processing.
Land Pix	Number of land pixels in granule.
Water Pix	Number of water pixels in granule
Water Adjacent Fire Pix	Number of fire pixels that are adjacent to one or more water pixels.
Cloud Adjacent Fire Pix	*Number of fire pixels that are adjacent to one or more cloud pixels.*
Unknown Pix	Number of pixels assigned a class of unknown in granule.
Land Cloud Pix	Number of land pixels obscure by cloud in granule.
Water Cloud Pix	Number of water pixels obscured by cloud in granule (always 0 since the internal cloud mask is not applied over water pixels)
Glint Pix	Number of pixels in granule contaminated with Sunglint.
Glint Rejected Pix	Number of tentative fire pixels that were rejected due to apparent Sunglint contamination
Coast Rejected Pix	Number of tentative fire pixels that were rejected due to apparent water contamination of the contextual neighborhood
Hot Surf Rejected Pix	Number of tentative fire pixels that were rejected as apparent hot desert surfaces
Day Pix	Number of day time pixel sin granule.
Night Pix	Number of night time pixels in granule
Satellite	Name of satellite (“Terra”or“Aqua”).
Process Version Number	Program version string (e.g. “5.0.1”).
MOD021KM input file	File name of MOD021KM (Terra) or MYD021KM (Aqua) Level 1B radiance input granule.
MOD03 input file	File name of MOD03 (Terra) or MYD03 (Aqua) relocation input granule.
System ID	Operating system identification string

Table 3.4: MODIS Level 2 fire product metadata stored as standard global HDF attributes (Source: Giglio, 18 February 2010)

Level 3 8-day comprises a Daily composite fire products (MOD14A1 Terra and MYD14A1 Aqua) (Table 3.5) and a Summary fire products (MOD14A2 Terra and MYD14A2 Aqua). Both products are files spanning one of the 460 MODIS files, of which 326 contain pixels. The products are 1 km gridded composites of the pixels detected in each grid cell but, the only difference between the two is that the Daily composite fire products has 24 hours compositing period and the Summary fire product has the same just over each 8- day.

Attribute Name	**Description**
Fire Pix	Number of 1-km tile cells containing fires (8-element array).
Cloud Pix	Number of 1-km tile cells assigned a class of cloud after compositing (8-element array).
Miss Pix	Number of 1-km tile cells lacking valid data (8-element array).
Unknown Pix	Number of 1-km tile cells assigned a class of unknown after compositing (8-element array).
MaxT21	Maximum band 21 brightness temperature (K) of all fire pixels in tile.
Process Version Number	Program version string (e.g. "5.1.3").
Start Date	Start date of 8-day time period spanned by product (YYYY-MMDD).
End Date	End date of 8-day time period spanned by product (YYYY-MMDD).
Horizontal Tile Number	Horizontal tile coordinate (H).
Vertical Tile Number	Vertical tile coordinate (V).

Table 3.5: MOD14A1 and MYD14A1 fire product meta data stored as standard global HDF attributes (Source: Giglio, 18 February 2010)

Moreover navigation of the tiled MODIS products (Giglio, 18 February 2010) in the sinusoidal projection can be performed using the forward and inverse mapping transformations described. We'll first need to define a few constants:

- R = 6371007.181m, the radius of the idealized sphere representing the Earth;
- T = 1111950 m, the width of each MODIS tile in the projection plane;
- X min = -20015109 m, the western limit of the projection plane;
- Y max = 10007555 m, the northern limit of the projection plane;
- w = T/1200 = 926.62543305 m, the actual size of a "1-km" MODIS sinusoidal grid cell

First, for forward mapping denote the latitude and longitude of the location (in radians) as φ and λ, respectively. First compute the position of the point on the global sinusoidal grid:

$$x = R\lambda\cos\varphi \quad (1)$$

$$y = R\varphi. \quad (2)$$

Next compute the horizontal (H) and vertical (V) tile coordinates, where $0 \le H \le 35$ and $0 \le V \le 17$:

$$H = \left[\frac{x - x\,\min}{T}\right] \quad (3)$$

$$V = \left[\frac{y\max - y}{T}\right] \quad (4)$$

Finally, compute the row (i) and column (j) coordinates of the grid cell with in the MODIS tile:

$$i = \left[\frac{(y\,\max - y) \bmod T}{w}\right] - 0.5 \quad (5)$$

$$j = \left[\frac{(x - x\,\min) \bmod T}{w}\right] - 0.5 \quad (6)$$

Note that for the 1-km MOD14A1 and MYD14A1 products (indeed, all 1-km MODIS products on the sinusoidal grid) $0 \le i \le 1199$ and $0 \le j \le 1199$.

Second, for inverse mapping they given the row (i) and column (j) in MODIS tile H, V. First compute the position of the center of the grid cell on the global sinusoidal grid:

$$x = (j + 0.5)\, w + HT + x\,\min \quad (7)$$

$$y = y\,\max - (i + 0.5)\, w - VT \quad (8)$$

Next compute the latitude φ and longitude λ at the center of the grid cell (in radians):

$$\varphi = \frac{y}{R} \quad (9)$$

$$\lambda = \frac{x}{R\cos\varphi} \quad (10)$$

Finally, another product of MODIS is the Climate Modeling Grid Fire Products (MOD14CMH, MYD14CMH) (Figure 3.3). The CMG fire products, (Giglio, 18 February 2010) are gridded statistical summaries of fire pixel with 0.5^0 spatial resolution (each layer is a 720 x 360 numeric area) (Table 3.6) for one calendar month (MOD14CMH/ MYD14CMH) and eight days (MOD14C8H/MYD14C8H). Also it has higher resolution 0.25^0. Moreover Terra and Aqua MODIS sensors detect for each pixel a number of specific monthly information, provided from the Global Monthly Fire Location product (MCD14ML). The information that provides (Giglio, 18 February 2010) is for the geographic location, date and some additional information for each pixel that distributed as a plain ASCII (text) file with spaces. (Table 3.7)

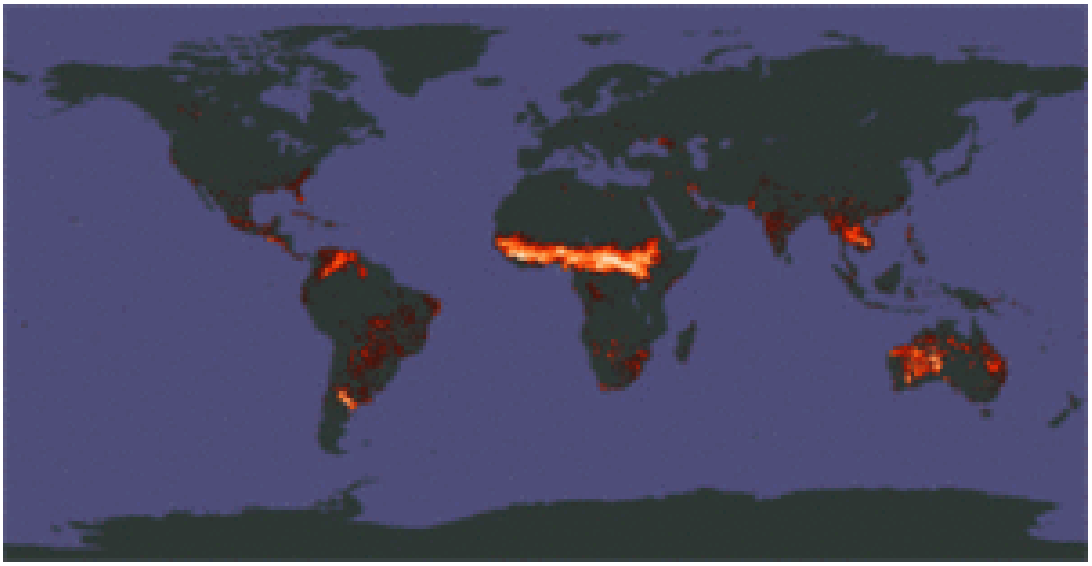

Figure 3.6: Example of CMG fire product. (Source: https://www.google.com.pg/search?q=Day+and+night+relationship+of+fire+size+and+fire+temperature&biw=1440&bih)

LayerName	DataType	Units	Description
CorrFirePix	int16	-	Correctednumberoffirepixels.
CloudCorrFirePix	int16	-	Corrected number of fire pixels, with an additionalcorrectionforcloudcover
MeanCloudFraction	int8	-	Meancloudfraction.
RawFirePix	int16	-	Uncorrectedcountoffirepixels.
CloudPix	int32	-	Numberofcloudpixels.
TotalPix	int32	-	Totalnumberofpixels.
MeanPower	float32	MW	Meanfireradiativepower.

Table 3.6: Summary of data layers in the CMG fire products. (Source: Giglio, 18 February 2010)

Column	Name	Units	Description
1	YYYYMMDD	-	UTC year (YYYY), month (MM), and day (DD).
2	HHMM	-	UTC hour (HH) and minute (MM).
3	sat	-	Satellite: Terra (T) or Qua (A).
4	lat	degrees	Latitude at center of fire pixel.

5	lon	degrees	Longitude at center of fire pixel.
6	T21	K	Band 21 brightness temperature of fire pixel.
7	T31	K	Band 31 brightness temperature of fire pixel.
8	sample	-	Sample number (range0-1353).
9	FRP	MW	Fire radiative power (FRP).
10	conf	%	Detection confidence (range 0-100).

Table 3.7: Summary of columns in the MCD14ML fire location product. (Source: Giglio, 18 February 2010)

In the next chapter the results achieved by applying RST and MOD14 for fore detection concerning the Crete and Attica will be shown and discussed.

CHAPTER 4: RESULTS

4.1 The investigated area: Crete and Attica

The geographical region of Crete includes the largest island of Greece and the fifth of Mediterranean, which along with the island that surrounds it occupies an area 8.323 km^2. Crete has 255km length and a maximum width of 12 to 55km, bordering from the north by the Cretan Sea (Figure 4.1) and from south by Libyan while the coastline is over 1000km. The geographical region of Crete includes four regional units, with the greater of Heraklion which occupies 31.7 % of the area of the compartment and after is Chania (28.5%), Lasithi (21.9%) and Rethimno (17.9%), (WWF, Ελλας/2012).

Figure 4.1: The location of Crete and Attica in Aegean Sea (Source: https://www.google.it/search?q=The+location+of+Crete+in+Aegean+Sea&espv=2&biw)

By geomorphological view Crete (Figure 4.2) described by the one of the most intense, with the 3/5 of the surface is mountainous-hilly (the higher, greater than 200m). The three major mountain ranges of the island, which are due on the existence of the fertile plateaus, are the White Mountains which reaches a height of 2.452 m above sea, the Ida mountain range (Mount Psiloritis) is the highest 2.456m, and Mount Dikti (Mountains of Lasithi) which is 2.148m that crosses in

order from the West to East. That which constitutes special characteristics of the Cretan environment is the wide variety of geological formations, caves, gorges and plateaus is a key component of Cretan landscape. Specifically, one of the most famous gorges is Samaria Gorge (16 km long), that from 1962 has been declared as National Park.

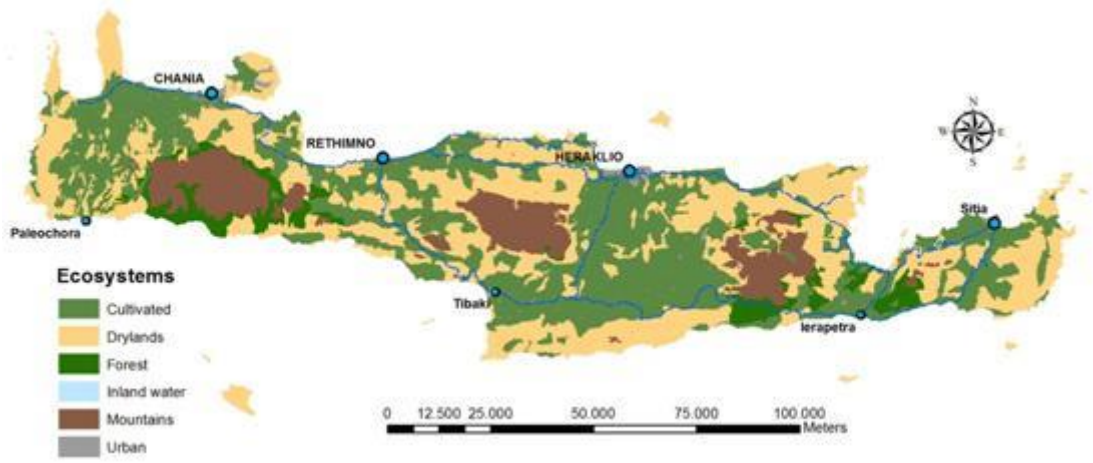

Figure 4.2 Geomorphology of Crete (Source: https://www.google.it/search?q=The+location+of+Crete+in+Aegean+Sea&espv=2&biw)

From climatological terms, Crete is part of the Mediterranean climate zone and imparts the principal character of climate, which is characterized as temperate. The atmosphere depending on the proximity to the sea is quite humid. The average annual temperature is greater in the east and south than in the west and in the north of the island. Moreover, the summer season where the average temperature is 25^0C to 30^0C, covers at least four months (June-September) with wormer in July. Winter on the other, is quite mild and wet with a lot of rainfall, mainly in the western part of the island. The snow is rare in the plains but quite often on mountains.

The natural environment of Crete is unique, because of its geographical position and isolating the flora introduced the highest endemism in Greece. In conclusion, the Crete contains 1.828 indigenous species, of which 189 are endemic to Crete and in the surrounding islands.

The next area that investigated was Attica. Attica is the historical area in Greece that includes the city of Athens which is also the capital city. It is a triangular peninsula that protrudes in the Aegean Sea (Figure 4.1), has an area of 3.808 km^2 and covers 2.9% of the total area of the country. The extent of the region of Attica is of the most lowlands of the country and the plains cover about 64% of the total area, the hilly 30% and the mountain the rest 6%. The highest mountain is Parthina (1.413 m), while very high also is Hymettus, Penteli, Pateras and Gerania. Moreover, in the east part (plain of Mesogeia) and south of Parnitha (Thriasio field) are found fertile plains, while in many other areas (Northeast and Southwest) the hill are very close to the sea

leaving only narrow strip of lowlands. The most characteristic physiographic feature is a basin, formed between Parnitha, Penteli, Hymittos, Aigaleo and Athos Poikilo, (Figure 4.3) of which rice almost vertically to three directions (North, West, and East) of Athens and suburbs with an area of approximately 220km^2. Therefore, the main "opening" of the basin is only in the south, where there is the Saronic Gulf and the small openings between Parnithas-Hymettus.

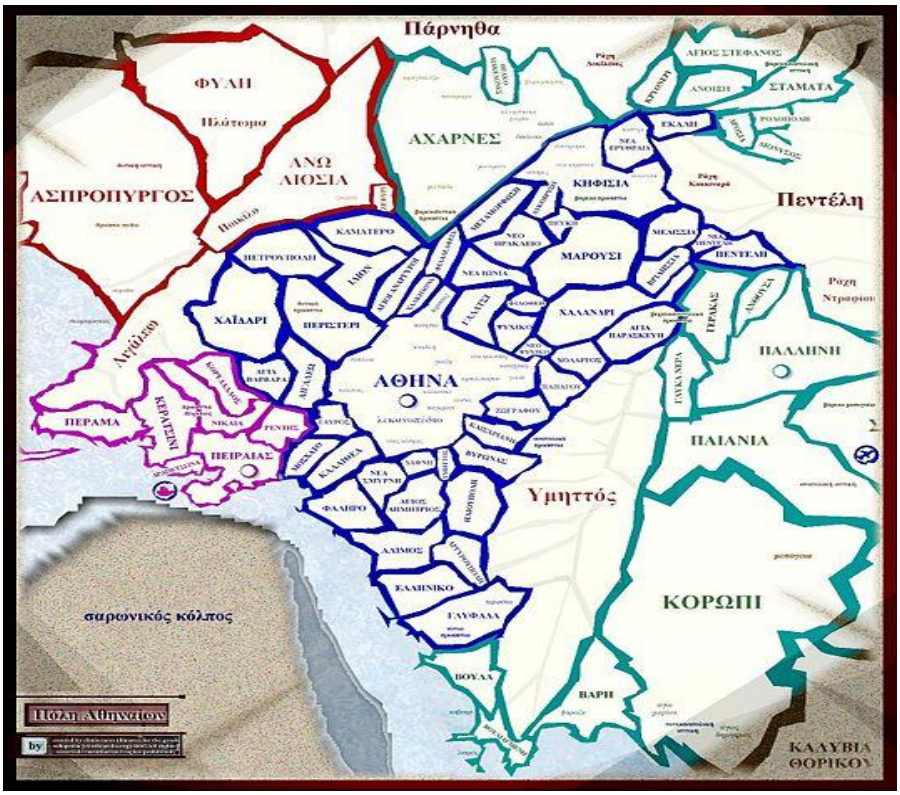

Figure 4.3: Basin formed between Parnitha, Penteli, Hymittos, Aigaleo and Athos Poikilo (Source: https://www.google.it/search &source=lnms&tbm=isch&sa=X&ved=0ahUKEwiNk9rYtMjOAhUJUhQKHRK1B0MQ_AUIBygC&dpr=1 #imgrc=GR3LpvHx4f3DtM%3A)

In Attica the climate is temperate, Mediterranean and generally mild in most of the time. Although it is Mediterranean, the climate of Athens has quite big difference in the findings of temperature between summer and winter than other areas of the country. The average annual temperature is 18.3 ^{0}C, but there are few times that the temperature exceeding 40^{0}C (heat). Specifically, the hottest month considered the July, while cooler is undoubtedly January. Athens is famous for the particular hot summers while the highest temperature on record is 48^{0}C on July 10, 1977. Finally, the snowfall and rainfall is rare during the year, specifically rainfall ranging from the end of September until mid-April.

4.2 RST and MOD14 implementation for the analysis of Crete and Attica.

Before going ahead with the analysis, following the procedures described in the previous chapter, i would like to emphasize that MODIS data (Collection 5) have been used. All data acquired in July from 2003 to 2015 available in the on-line archive of the Institute of Methodologies for Environmental Analysis (IMAA) of the National Research Council (CNR), Tito Scalo (PZ). After of these available data was selected to be analyzed July 2007, because as I mentioned in the first chapter, this year and moth was one of the biggest disasters in the history of modern Greece. About the year of validation (July 2007), MODIS data that were not available in IMAA-CNR archive were downloaded from LAADS (Level 1 and Atmosphere Archive and Distribution System) (https://ladsweb.nascom.nasa.gov/). All data were calibrated in terms of reflectance (VIS, channel 01) or brightness temperature (MIR, channels 21, 22; TIR, channels 31, 32). For each image, sensor zenith information was extracted, too. At the same time, data were geo-located and the area shown in Figure 4.4 was extracted.

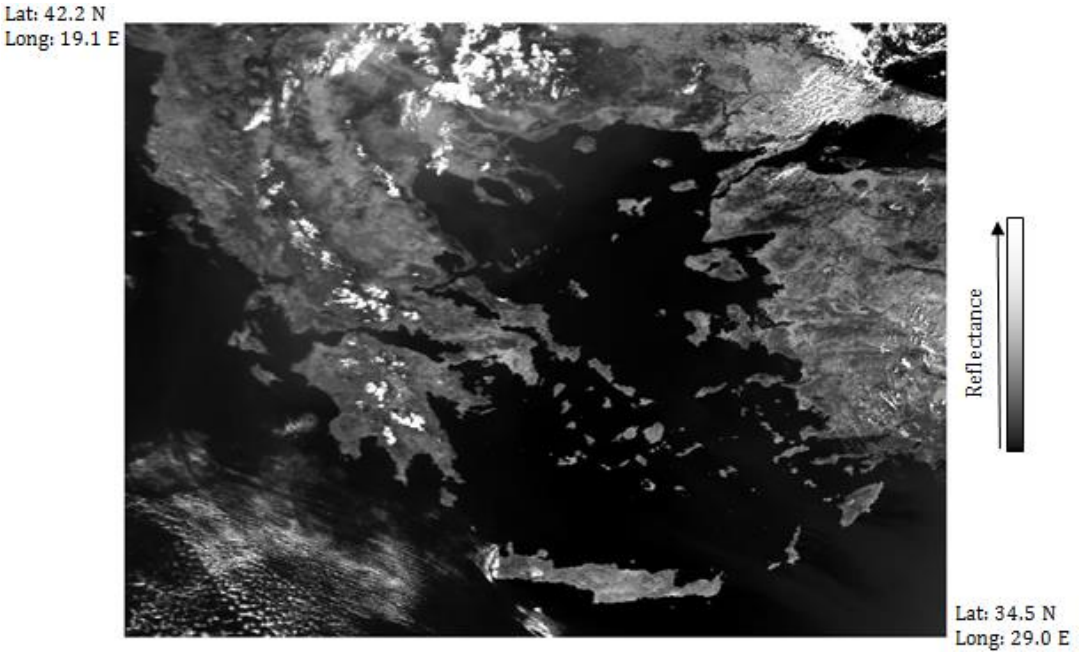

Figure 4.4: Investigated area extracted from MODIS orbit data (VIS, 31/07/2007 08:55 GMT, MODIS/Terra)

4.2.1 Reference field computation

The second processing step was the calculation of reference fields. The computation of reference fields as I mentioned on previous chapter, was based on RST (Robust Satellite Techniques), which is an algorithm that analyze multi-year historical series of homogeneous satellite records (i.e. same month of year, at same hour of the day), for the identification of signal normal behavior at pixel level. Specifically, deal with the implementation of a local variation index

ALICE (Absolutely Local Index of Change of Environment) that estimates at pixel level how much the satellite signal at time t deviates from normal behavior.

$$\otimes_{\mathrm{V}}(\mathrm{x},\mathrm{y},\mathrm{t}) = \frac{[V(x,y,t) - \mu_V(x,y)]}{\sigma_{\mathrm{V}}(\mathrm{x},\mathrm{y})}$$

Where V(x, y, t) is the satellite signal measured at time t in a specific spectral band (or it is a combination of more spectral bands) at location (x, y), while $\mu_V(x,y)$ represent the temporal mean and $\sigma_{\mathrm{V}}(\mathrm{x},\mathrm{y})$ the standard deviation of the same signal V(x, y) at the same location (x, y), calculated using multi-year historical series of homogeneous cloud free satellite records.
In this case, only pixels with sensor zenith < 40° have been considered in the reference field computation.

Moreover, the available data from the preprocessing that used for the calculation of reference fields, for July 2003 to 2015were considered for an amount of 10.468 images, about 34 Gbytes (Table 4.1). Some data also, were separated considering the Earth Observing System (EOS) (http://eospso.nasa.gov/ platform) (Aqua, Terra), which is a coordinated series of polar-orbiting and low inclination satellites for long-term global observations of the land surface, biosphere, solid Earth, atmosphere, and oceans, time of acquisition (daytime, nighttime) and channels. Generated reference fields are summarized in Table 4.2.Where, during the computation of MIR-TIR was applied cloud detection based on VIS (only in daytime) and TIR (both daytime and nighttime).
A pixel is flagged as "cloudy" if:

$$\otimes_{ch01}(x,y,t) \equiv \frac{R_{ch01}(x,y,t) - \mu_{ch01}(x,y)}{\sigma_{ch01}(x,y)} \quad >2$$

OR

$$\otimes_{ch32}(x,y,t) \equiv \frac{T_{ch32}(x,y,t) - \mu_{ch32}(x,y)}{\sigma_{ch32}(x,y)} \quad < -2$$

Table 4.1: Number of images used in reference field computation for each channel, EOS platform and year of acquisition.

Platform	Channel	2003	2004	2005	2006	2007	2008	2009	2010	2011	2012	2013	2014	2015	TOT
Aqua	ch01	47	47	49	34	44	47	23	29	27	14	46	45	45	**497**
	ch21	104	104	104	76	98	99	59	71	64	42	102	105	100	**1128**
	ch22	104	104	104	76	98	99	59	71	64	42	102	105	100	**1128**
	ch31	104	104	104	76	98	99	59	71	64	42	102	105	100	**1128**

	ch32	104	104	104	76	98	99	59	71	64	42	102	105	100	**1128**
Terra	ch01	58	58	55	56	54	54	33	37	37	30	52	57	54	**635**
	ch21	108	107	105	111	100	102	65	72	69	61	101	104	101	**1206**
	ch22	108	107	105	111	100	102	65	72	69	61	101	104	101	**1206**
	ch31	108	107	105	111	100	102	65	72	69	61	101	104	101	**1206**
	ch32	108	107	105	111	100	102	65	72	69	61	101	104	101	**1206**
Total		**953**	**949**	**940**	**838**	**890**	**905**	**552**	**638**	**596**	**456**	**910**	**938**	**903**	**10468**

Table 4.2: Reference fields together with other specific information used for their computation

Reference field group	**Reference fields**	**Used channels**	**Clipping**				**Purpose**
			Starting value daytime	**Starting value nighttime**	**kσ-clipping**	**Symmetric/ asymmetric clipping**	
Single channels	μ_{ch01}, σ_{ch01} *for Aqua and Terra, only daytime*	01 (VIS, 0.620-0.670 μm)	15% (reflectance)	----------	2	Symmetric	Cloud detection
	μ_{ch21}, σ_{ch21} *for Aqua and Terra, daytime and nighttime*	21 (MIR, 3.929-3.989μm)	280 K	270 K	2	Symmetric	Hot spot detection
	μ_{ch22}, σ_{ch22} *for Aqua and Terra, daytime and nighttime*	22 (MIR, 3.929-3.989 μm)	280 K	270 K	2	Symmetric	Hot spot detection
	μ_{ch32}, σ_{ch32} *for Aqua and Terra, daytime and nighttime*	32 (TIR, 11.770-12.270 μm)	275 K	270 K	2	Symmetric	Cloud detection
Difference of channels	$\mu_{ch21-31}$, $\sigma_{ch21-31}$ *for Aqua and Terra, daytime and nighttime*	21-31	----------	----------	---------- -	----------	Hot spot detection
	$\mu_{ch22-31}$, $\sigma_{ch22-31}$ *for Aqua and Terra, daytime and nighttime*	22-31	----------	----------	---------- -	----------	Hot spot detection

Follow figures show some examples of reference fields (both single channel and difference of channels; nighttime and daytime; Terra and Aqua satellites) are in Figure 4.5 (channel 01), Figure 4.6 (channel 21), Figure 4.7 (channel 22), Figure 4.8 (channel difference 21-31), Figure 4.9 (channel difference 22-31), and Figure 4.10 (channel 32).

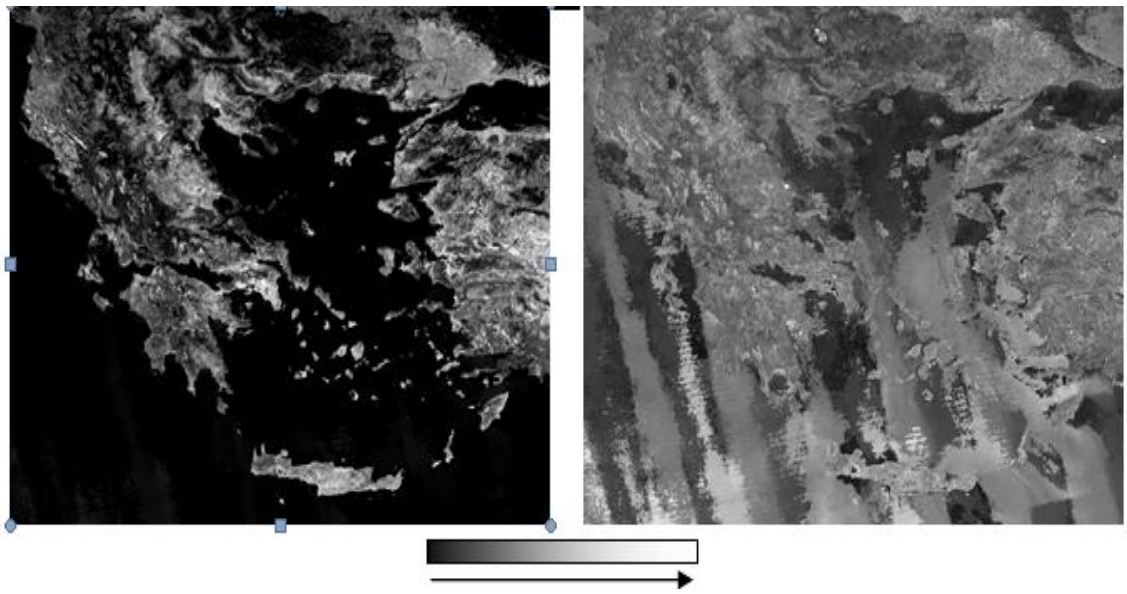

Figure 4.5: Example of July channel 01 (VIS, 0.62-0.67 μm) reference fields (Aqua platform). Left: mean (μ_{ch01}); right: standard deviation (σ_{ch01}).

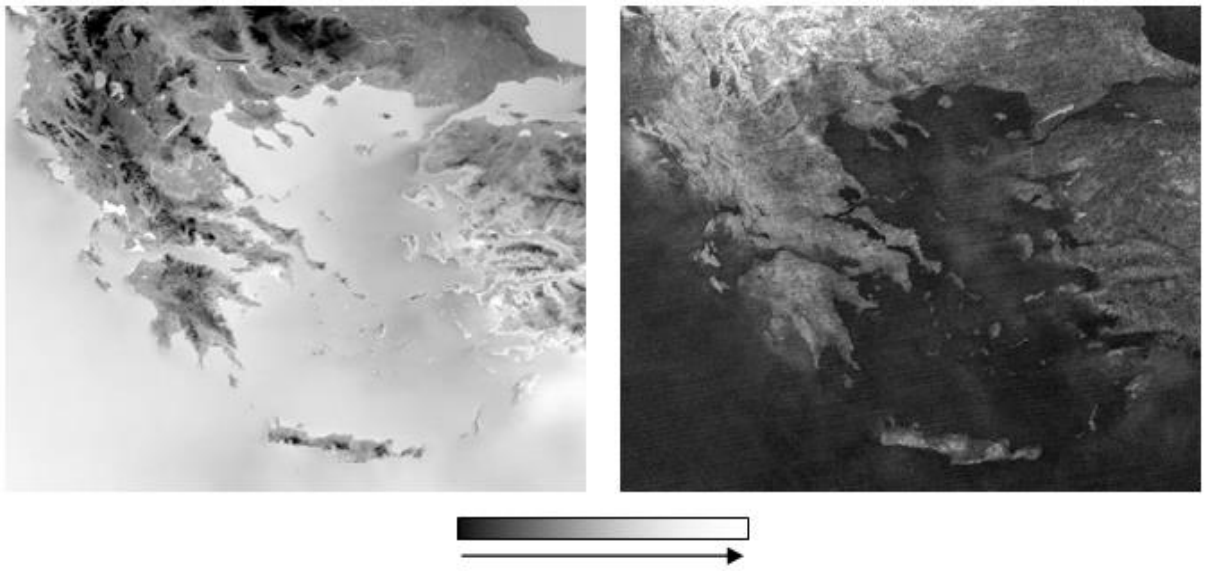

Figure 4.6: Example of July channel 21 (MIR, 3.929-3.989μm) night-time reference fields (Terra platform). Left: mean (μ_{ch21}); right: standard deviation (σ_{ch21}).

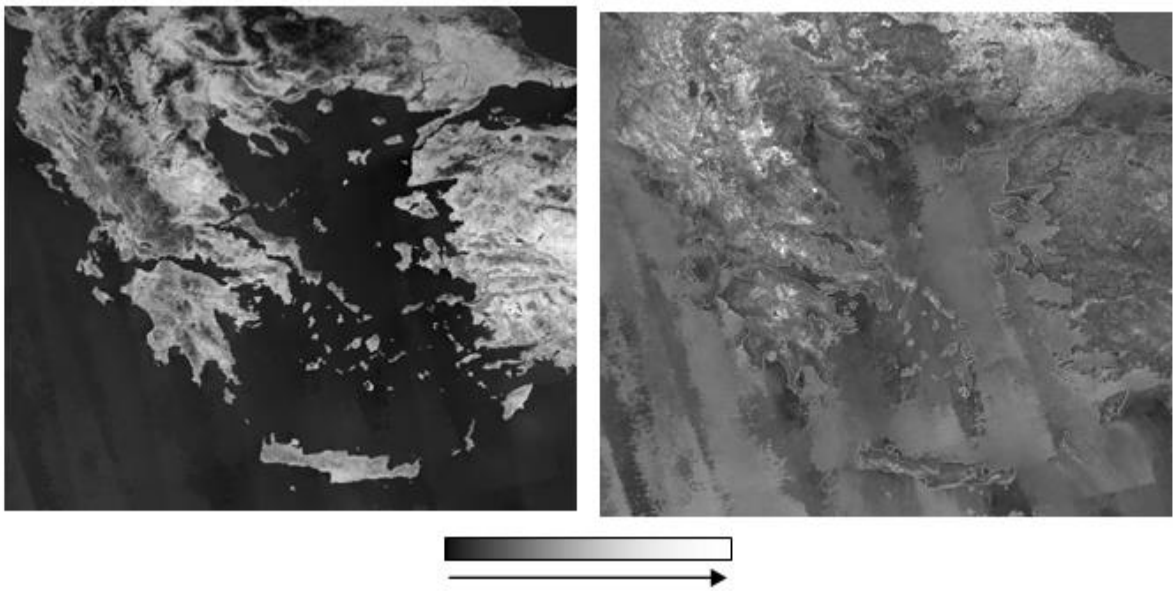

Figure 4.7: Example of July channel 22 (MIR, 3.929-3.989μm) daytime reference fields (Aqua platform). Left: mean (μ_{ch22}); right: standard deviation (σ_{ch22}).

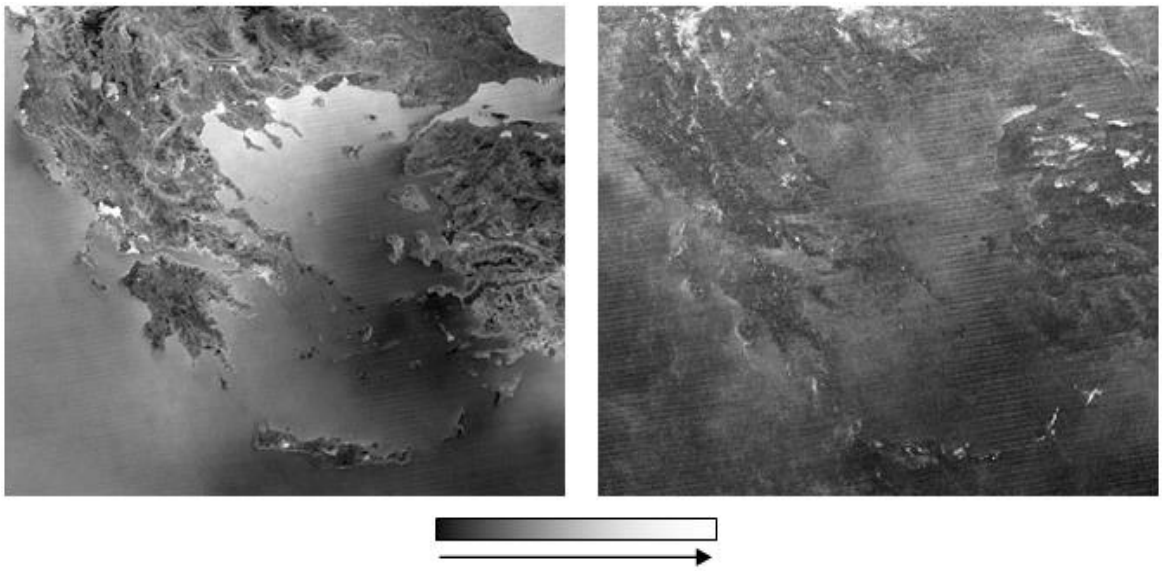

Figure 4.8: Example of July channel 21-31 (MIR – TIR) night-time reference fields (Terra platform). Left: mean ($\mu_{ch21-31}$); right: standard deviation ($\sigma_{ch21-31}$).

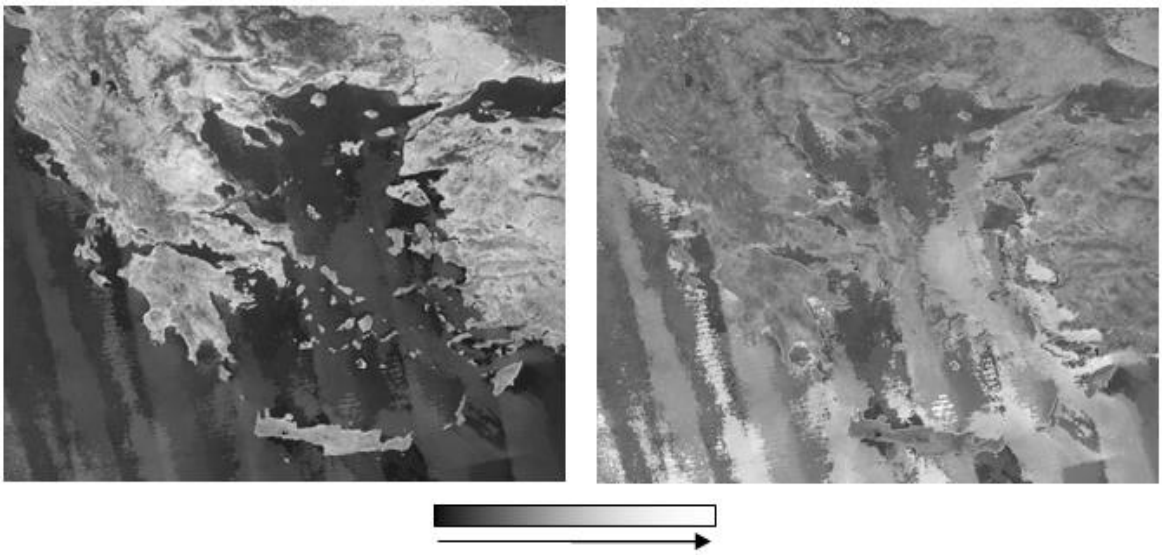

Figure 4.9: Example of July channel 22-31 (MIR – TIR) daytime reference fields (Aqua platform). Left: mean ($\mu_{ch22-31}$); right: standard deviation ($\sigma_{ch22-31}$).

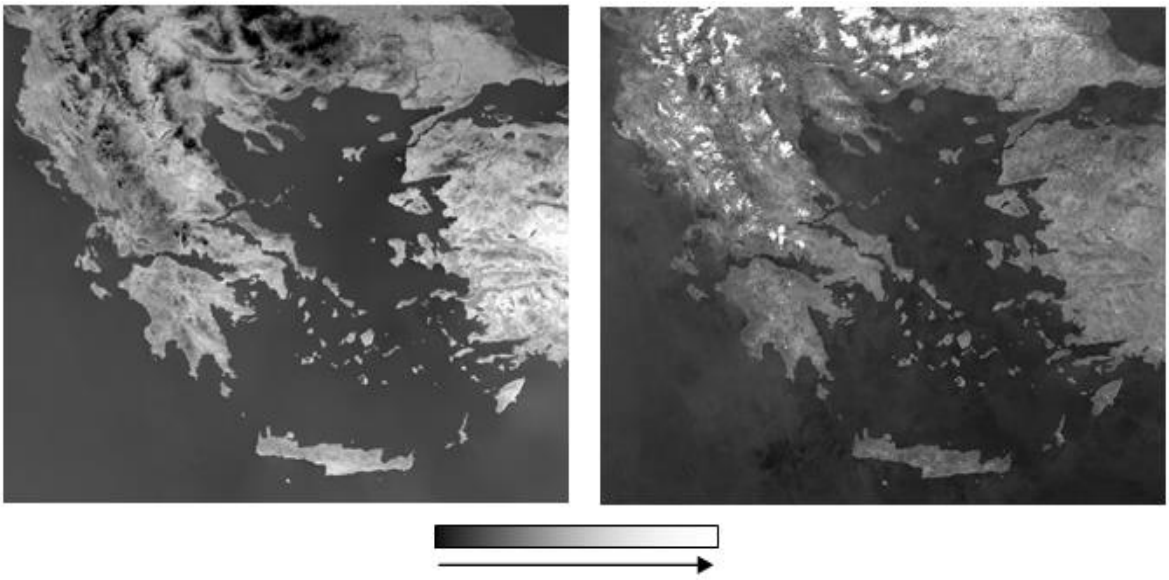

Figure 4.10: Example of July channel 32 (TIR, 11.770-12.270μm) daytime reference fields (Aqua platform). Left: mean (μ_{ch32}); right: standard deviation (σ_{ch32}).

4.2.2 Thermal anomalies computation

The calculation of the Reference fields that analyzed in the previous step was held for the computation of thermal anomalies. Before computing thermal anomalies, a cloud detection phase is performed, following the same tests as in MIR-TIR reference field computation (see above). Then, a RST-FIRES thermal anomaly is detected if:

$$\otimes_{ch22}(x,y,t) \equiv \frac{T_{ch22}(x,y,t) - \mu_{ch22}(x,y)}{\sigma_{ch22}(x,y)} > 3 \quad \text{AND} \quad \otimes_{ch22-31}(x,y,t) \equiv \frac{T_{ch22-31}(x,y,t) - \mu_{ch22-31}(x,y)}{\sigma_{ch22-31}(x,y)} > 3$$

In case of pixel saturation (Tb_{ch22}=331K), the following tests are used in place of the previous ones:

$$\otimes_{ch21}(x,y,t) \equiv \frac{T_{ch21}(x,y,t) - \mu_{ch21}(x,y)}{\sigma_{ch21}(x,y)} > 3 \quad \text{AND} \quad \otimes_{ch21-31}(x,y,t) \equiv \frac{T_{ch21-31}(x,y,t) - \mu_{ch21-31}(x,y)}{\sigma_{ch21-31}(x,y)} > 3$$

A filter was used to exclude thermal anomalies along coast lines in case of discrepancy between the land/sea mask associated to MODIS data and the land/sea mask generated on the basis of ancillary information.

4.2.3 Validation

Validation of the RST-FIRES algorithm was performed on the basis of 194 documented events. The occurrence of 193 of such events is registered in a database downloaded from (http://data.gov.gr/). This database contains also information about starting and extinguishing times, municipality/address where each fire occurred, and land cover of burned areas. However, in many cases (about 45%) fire position is not so clear and it was not possible to perform the sensitivity analysis for such fires.

Just in one case, the presence of a fire was confirmed exploiting the high temporal repetition rate (15 min) of MSG-SEVIRI (Meteosat Second Generation- *Spinning* Enhanced Visible and Infrared Imager) sensor data. Figure 4.11a shows the area where RST-FIRES and MOD14/MYD14 detected a series of thermal anomalies during the night between 13 and 14 July 2007 as well as in the morning of 14 July 2007. Analyzing the SEVIRI signal (in terms of brightness temperature) measured in the MIR channel (3.9 μm), from 13 July 00:00 GMT to 14 July 2007 23:45 GMT, an abrupt change clearly highlights the start of a fire between 22:00 and 22:15 GMT on 13 July (Figure 4.11b).

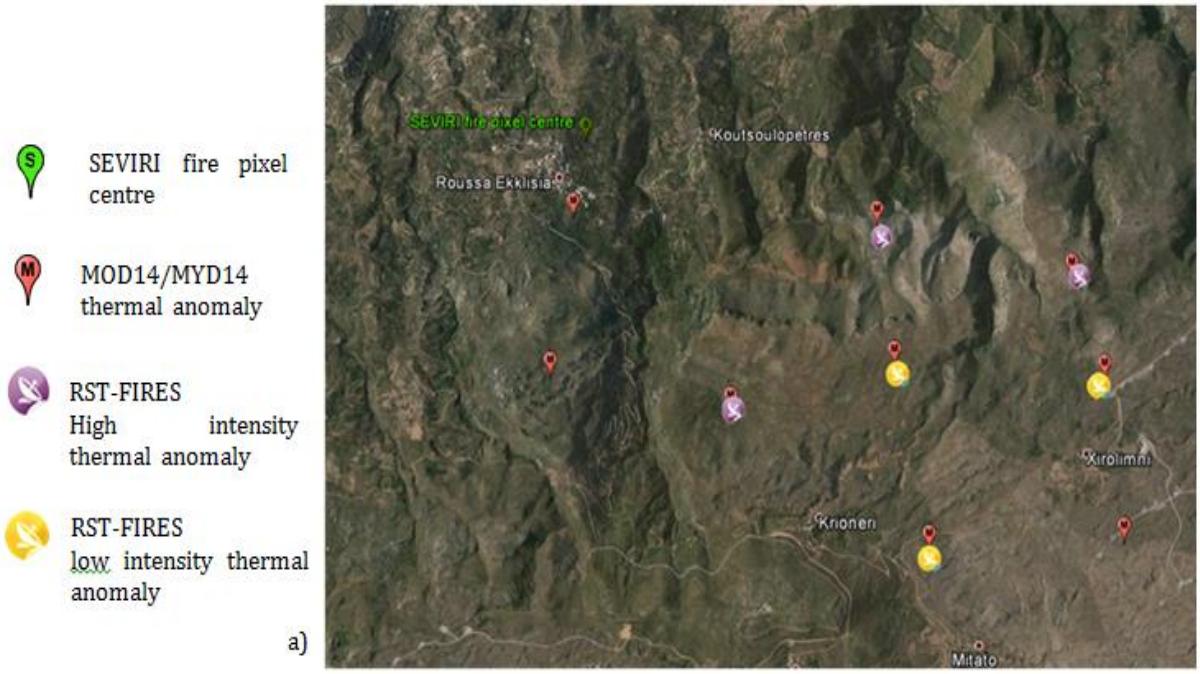

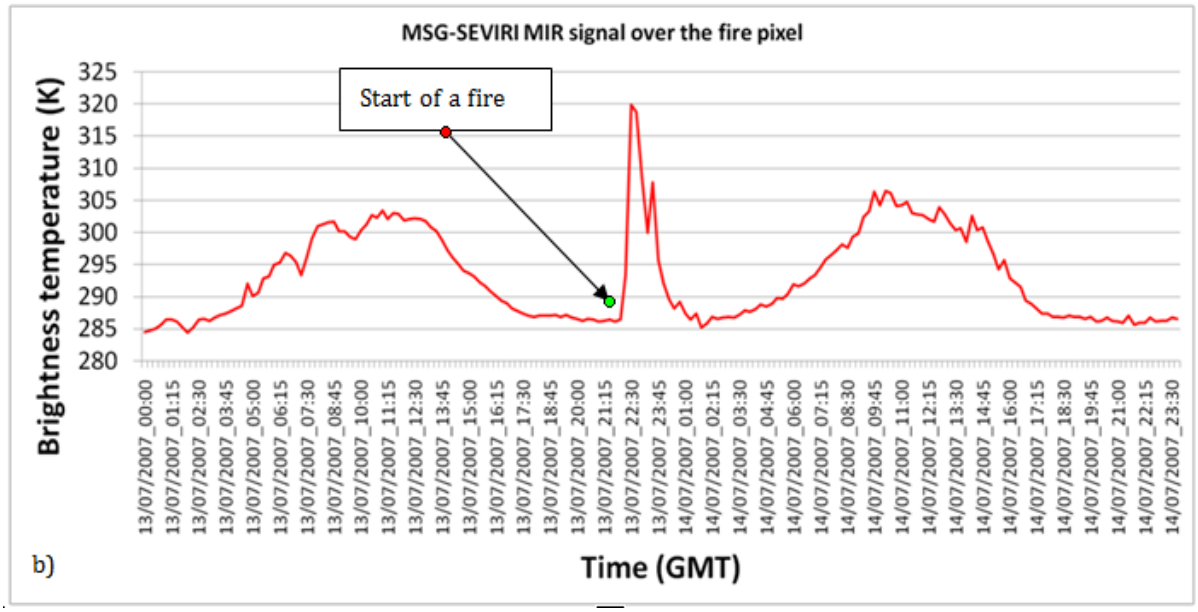

Figure 4.11: a) Thermal anomalies detected on MODIS images by MOD14/MYD14 and RST-FIRES between 13 and 14 July 2007 in the area of Roussa Church (no fire occurrence is documented in such an area within the used fire database). SEVIRI fire pixel centre is also indicated. b) Brightness temperature measured by SEVIRI in the MIR channel, in correspondence to the pixel indicated in a), from 13 July 2007 00:00 GMT to 14 July 2007 23:45 GMT. It is clear the abrupt change between 22:00 and 22:15 GMT on 13 July that highlights the start of a fire.

4.3 RST-FIRES sensitivity

As already pointed out, it was not possible to find the position of a great number of fires. The sensitivity analysis (Figure 4.12) was so performed only considering documented events with known position (55% out of the total). Moreover, 41% (i.e. 43/106) of fires with known position resulted to be not observable by MODIS sensor due to the presence of a cloud cover over the area affected by fires or due to the lack of Aqua/Terra passages between starting and extinguishing time of fires.

Concerning observable fires, 30% (i.e. 19/63) were successfully identified by RST-FIRES. Most of these fires were detected with more than one thermal anomaly. In the case of the fire which occurred in the Hydra Island (Prefecture of Attica) from 24 July to 3 August 2007, 45 thermal anomalies were recorded between 25 and 31 July 2007.

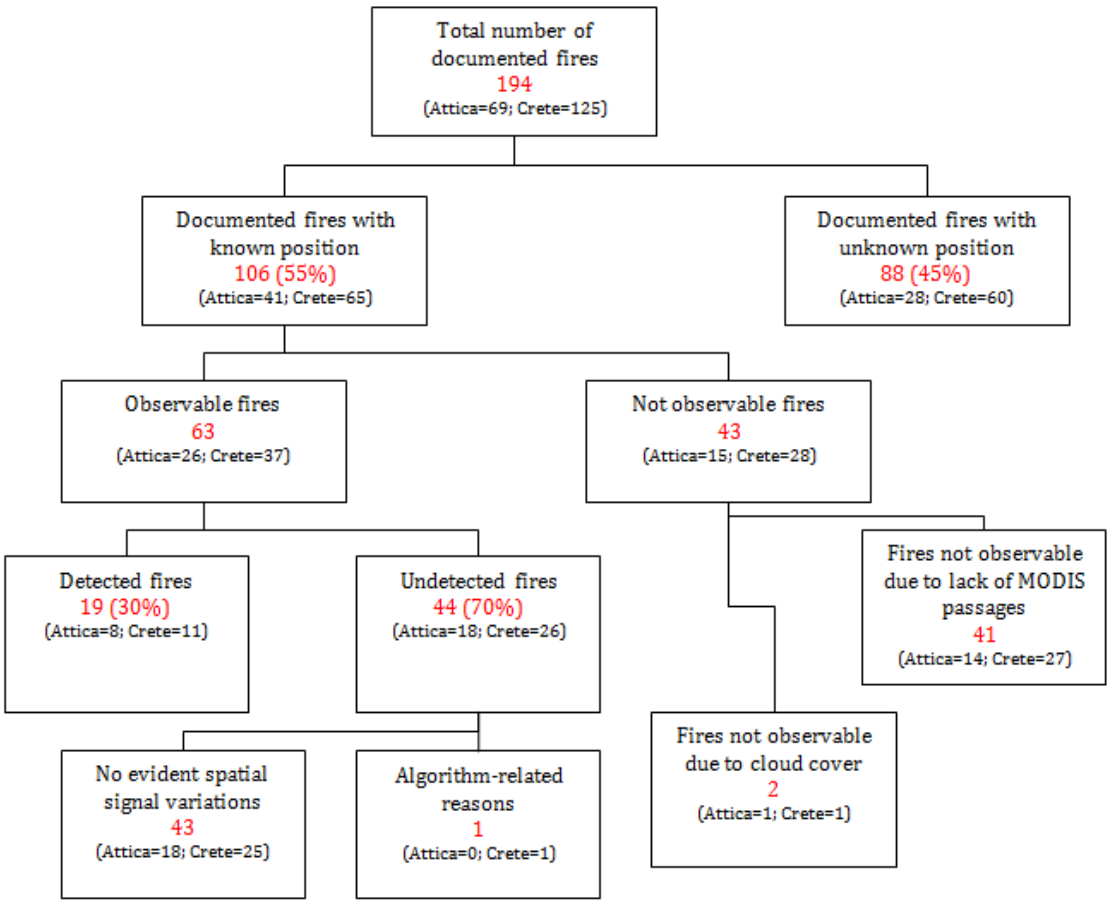

Figure 4.12: Sensitivity analysis overview

The RST-FIRES success rate (30%) could appear quite low, but looking at the burned areas corresponding to the successfully identified fires (Figure 4.13, Figure 4.14, and Figure 4.15), it is evident that within this percentage the most disastrous fires are included.

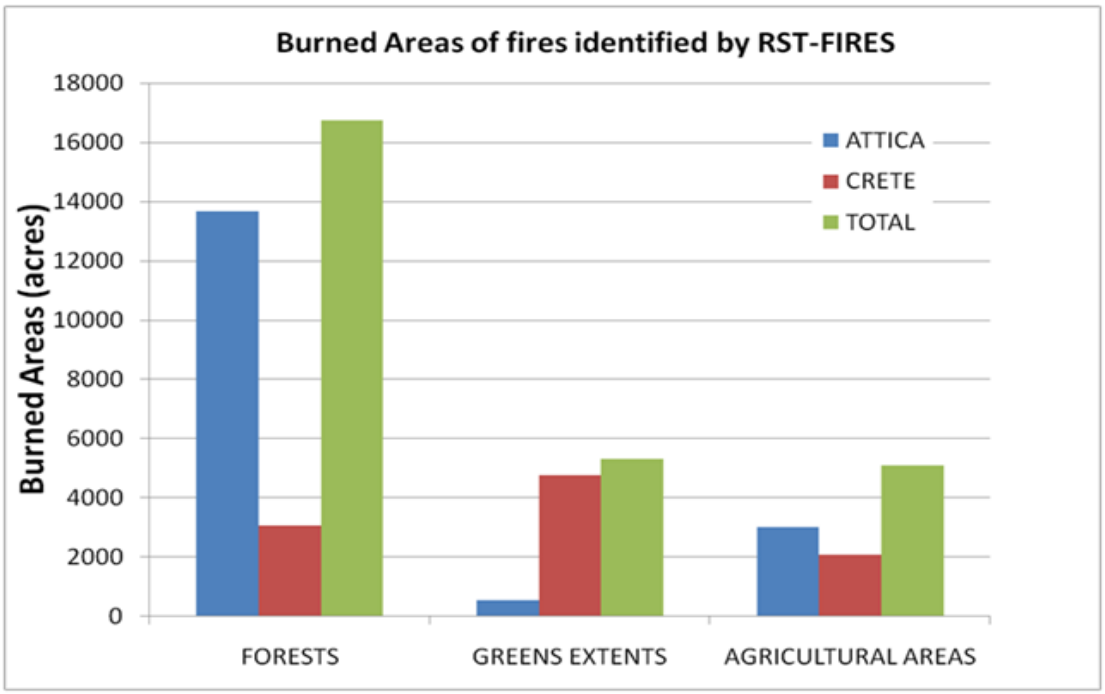

Figure 4.13: Burned areas of fires successfully identified by RST-FIRES, considering separately fires in Attica and Crete as well as the total.

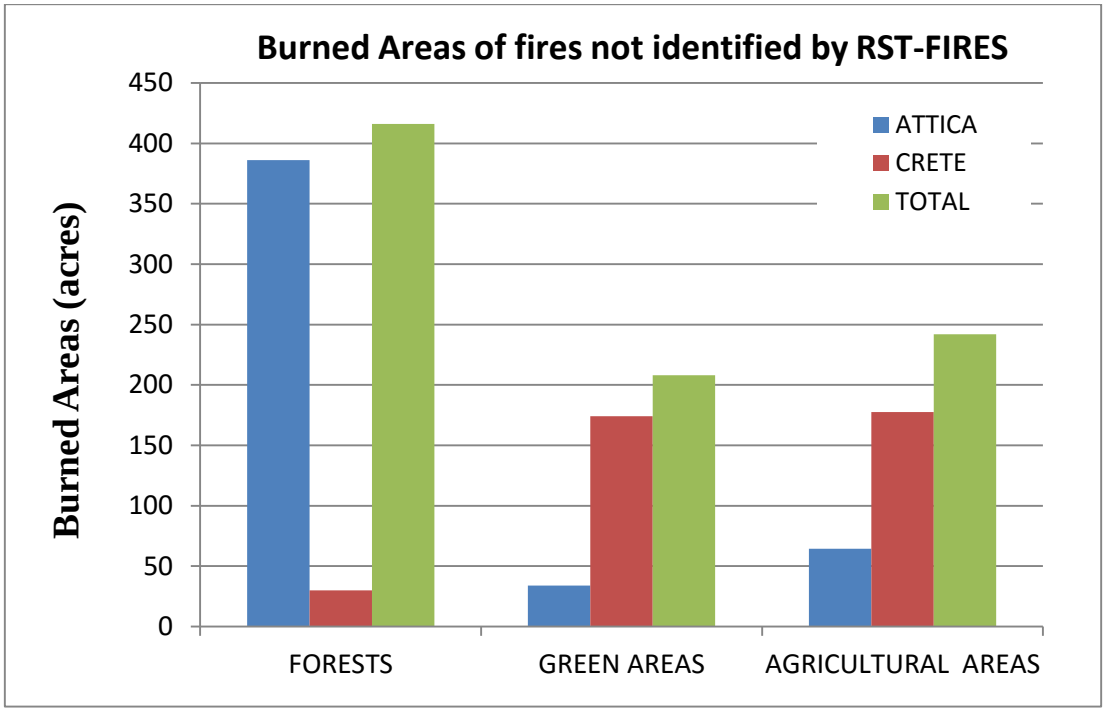

Figure 4.14: burned areas of fires that were not identified by RST-FIRES, considering separately fires in Attica and Crete as well as the total.

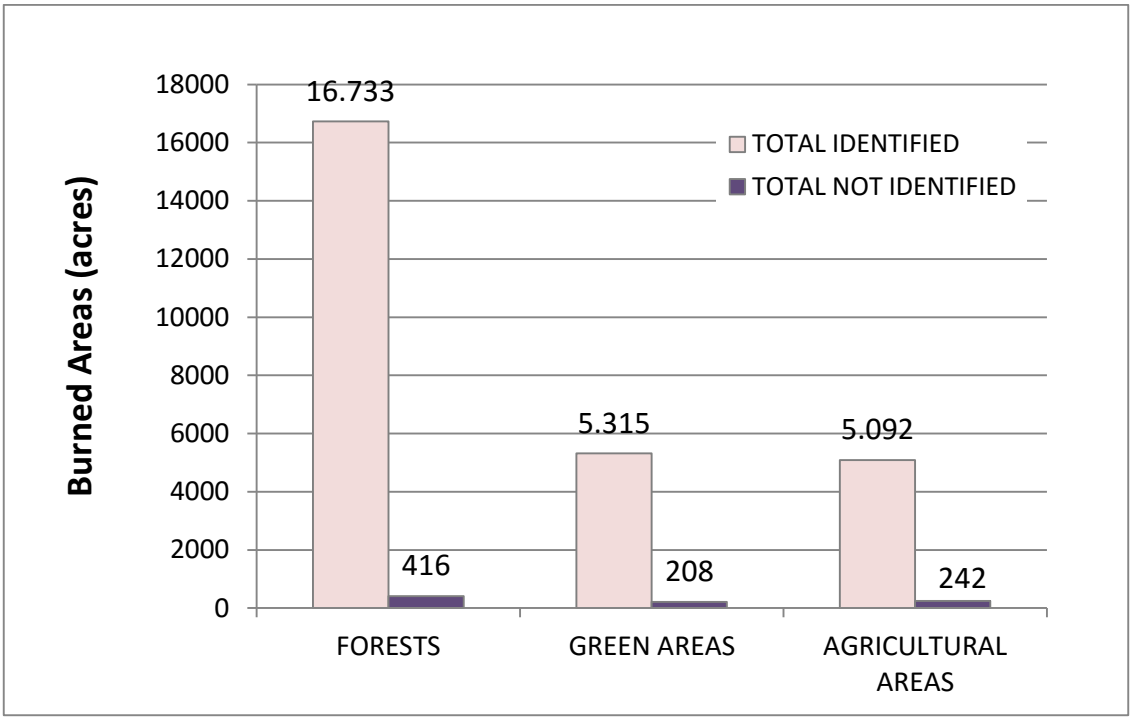

Figure 4.15: Total burned areas of identified vs. not identified fires.

The RST-FIRES success rate is also significant if compared with the performance of other MODIS-based fire detection products. To this aim, a comparison was made between RST-FIRES and MOD14/MYD14 (Giglio et al., 2003) which is the most used MODIS-based fire detection product at a global level.

RST-FIRES appear to be more sensitive than MOD14/MYD14, both in terms of detected events and thermal anomalies associated to documented events (Table 4.3, Figure 4.16, and Figure 4.17).

Table 4.3: Validation results

	ATTICA		CRETE		TOT	
Observable fires	26		37		63	
MODIS-based fire product	RST-FIRES	MOD14/ MYD14	RST-FIRES	MOD14/ MYD14	RST-FIRES	MOD14/MYD14
Identified events	8 (31%)	7 (27%)	11 (30%)	9 (24%)	19 (30%)	16 (25%)
Thermal anomalies associated to documented events	62	28	42	39	104	67

Thermal anomalies not associated to documented events	71	1	39	0	110	1

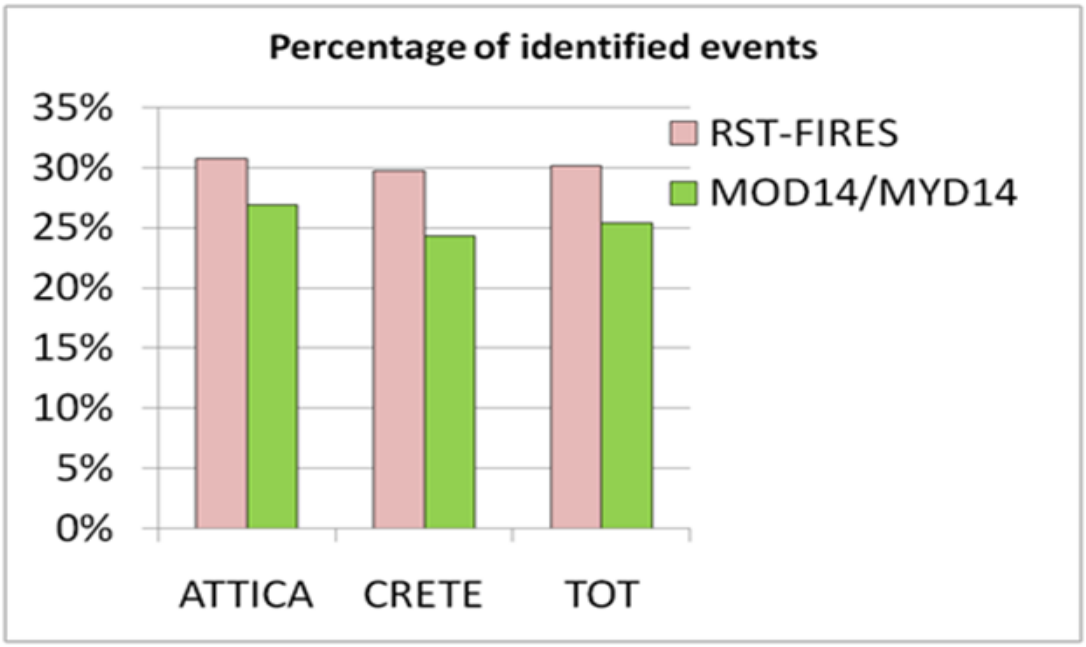

Figure 4.16: Percentage of events identified by RST-FIRES and MOD14/MYD14

.

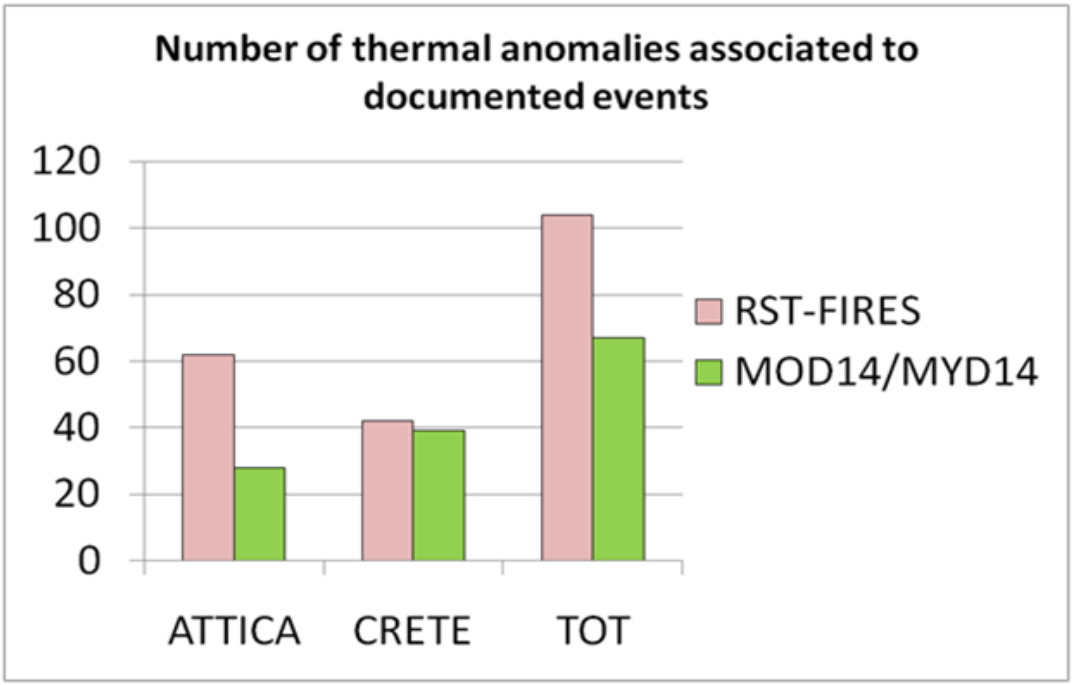

Figure 4.17: Number of thermal anomalies identified by RST-FIRES and MOD14/MYD14 which are associated to documented events.

A deeper analysis was performed in order to verify the reason why 70% of observable fires were undetected. MIR and TIR MODIS images were inspected in correspondence to the position of the undetected documented fires. In almost all cases (98%, i.e. 43/44), no evident spatial MIR signal variations were so evident to highlight the presence of a fire. Just in one case (a fire in the Prefecture of Rethymno, occurred on 2 July 2007), MIR signal variations were evident (Figure 18a) and associable to the presence of a fire.

A focused analysis showed that the fire was not detected due to low values of the $\otimes_{ch22}$ index despite high values of the $\otimes_{ch22-31}$ index. Figure 4.18b-c shows the MIR (T_{ch22}) and MIR-TIR ($T_{ch22-31}$) signals along the transect A-B of Figure 4.18a. Expected values (μ_{ch22}, $\mu_{ch22-31}$) and related normal variability ($\mu_{ch22} \pm 3\sigma_{ch22}$, $\mu_{ch22-31}$, $\pm 3\sigma_{ch22-31}$) are also indicated together with each own signal. In the case of the MIR signal, an abrupt change is clearly visible in correspondence to the fire, but MIR values remain within the normal variability so that the $\otimes_{ch22}$ index assumes low values (around zero). Differently from MIR, the abrupt change of the MIR-TIR signal is beyond its normal variability so that the $\otimes_{ch22-31}$ index assumes high values (around 6). Not with standing this, no thermal anomaly was detected because the present RST-FIRES configuration requires high values (see tests above) for both of the indices.

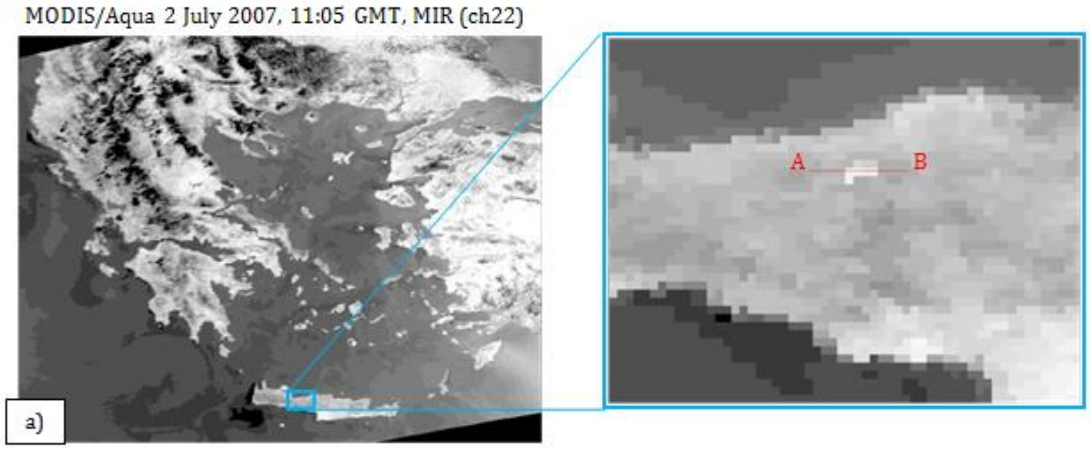

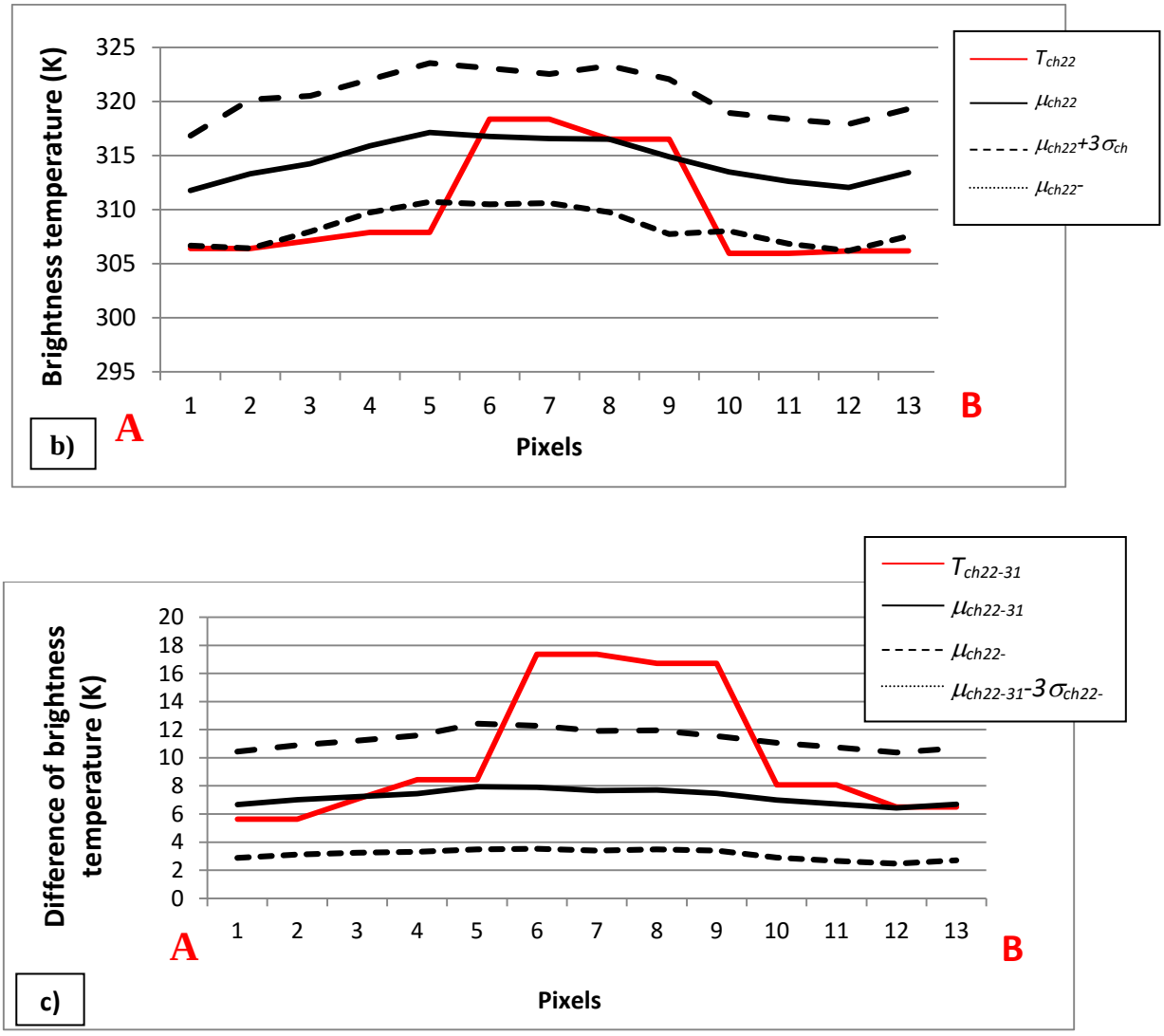

Figure 4.18: Fire in the Prefecture of Rethymno (2 July 2007). a) MIR MODIS image over the whole Greece (left) and zoom over the area affected by the fire (right). It is evident a MIR signal spatial variation in the fire area. b) MIR signal along the transect A-B compared with its expected value (μ_{ch22}) and normal variability ($\mu_{ch22} \pm 3\sigma_{ch22}$). Even if MIR signal clearly shows an abrupt change in correspondence to the fire, its values are within the range of its normal variability. c) Unlike MIR, the MIR-TIR signal excess ($T_{ch22-31} - \mu_{ch22-31}$) in the area of the fire is up to six times $\sigma_{ch22-31}$.

4.4 RST-FIRES reliability

A large number of false alarms were identified by RST-FIRES particularly in the last decade of July (Figure 4.19). In particular, about 87% (i.e. 96/110) of thermal anomalies, which were not associated to any documented event, were registered from 22 to 31 July 2007.

A deeper analysis revealed that this great number of false alarms is concomitant with a heat wave that affected Greece in the last decade of July 2007(Tolika et al., 2009; Theoharatosa et al.,

2010). The warming at the end of July is also evident if we consider the values measured in MIR (ch22) by MODIS onboard Aqua platform in nighttime passages over an area affected by such a heat wave, as compared with its expected value (μ_{ch22}) and it normal variability (σ_{ch22}) (Figure 4.20). The same is evident considering TIR (ch31) (Figure 4.21).

It should be noted that the use of $\otimes_{ch22-31}$ in combination with $\otimes_{ch22}$ is able to protect from false alarm proliferation in most of the cases, but it is not enough in case of very extreme warming (Figure 4.22).

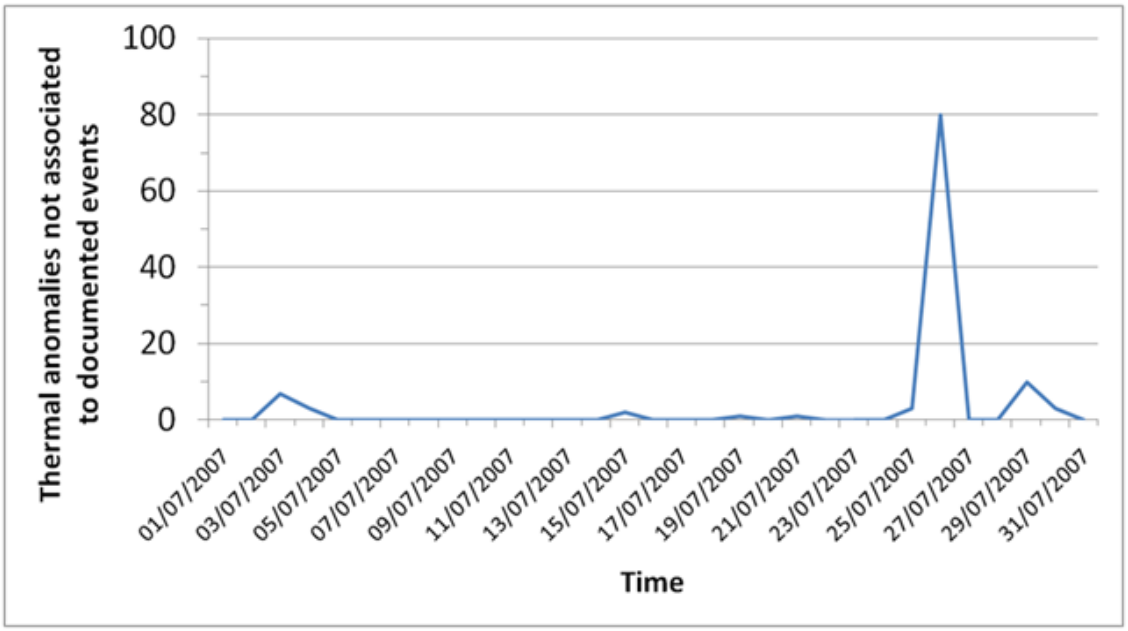

Figure 4.19: Number of thermal anomalies which are not associated to documented events, day-by-day.

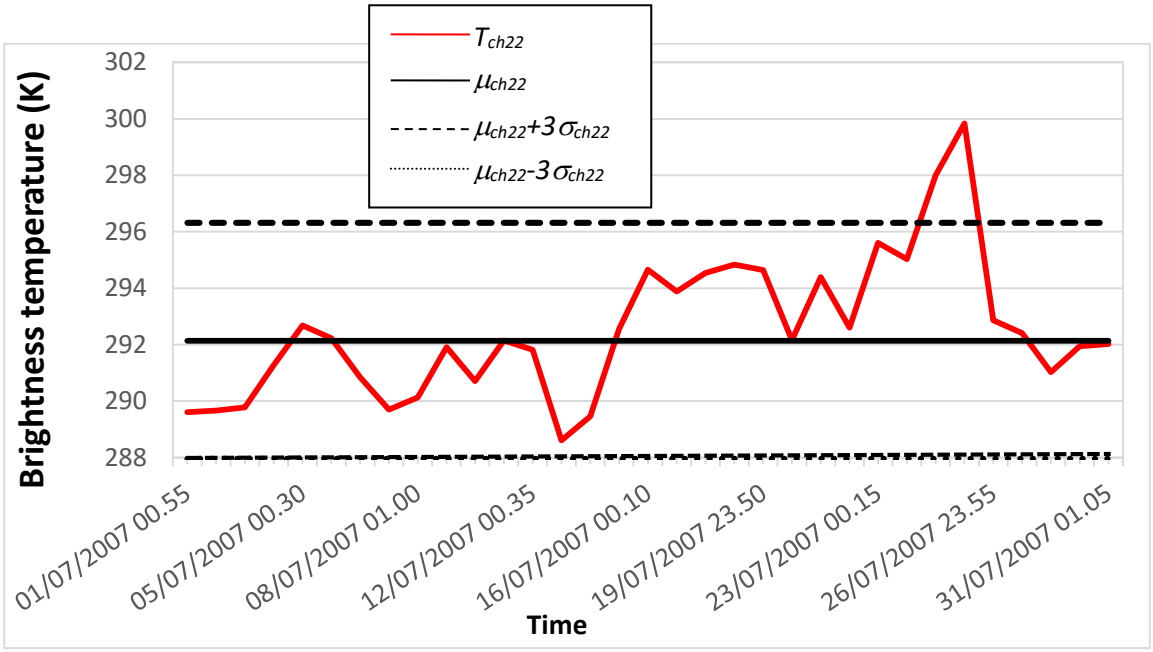

Figure 4.20: MIR signal (T_{ch22}) measured by MODIS instrument onboard Aqua platform in channel 22 during July 2007 nighttime passages over an area affected by a false alarm proliferation (MODIS pixel centered at 36.235 N, 22.985 E), together with the expected value (μ_{ch22}) and its normal variability ($\mu_{ch22} \pm 3\sigma_{ch22}$) over the same area, in the same period of the year and time of the day. Mean and standard deviation were computed on the basis of a historical dataset of nighttime MODIS/Aqua images from 2003 to 2015. The high values at the end of July are concomitant with the heat wave which affected Greece in the last decade of July 2007.

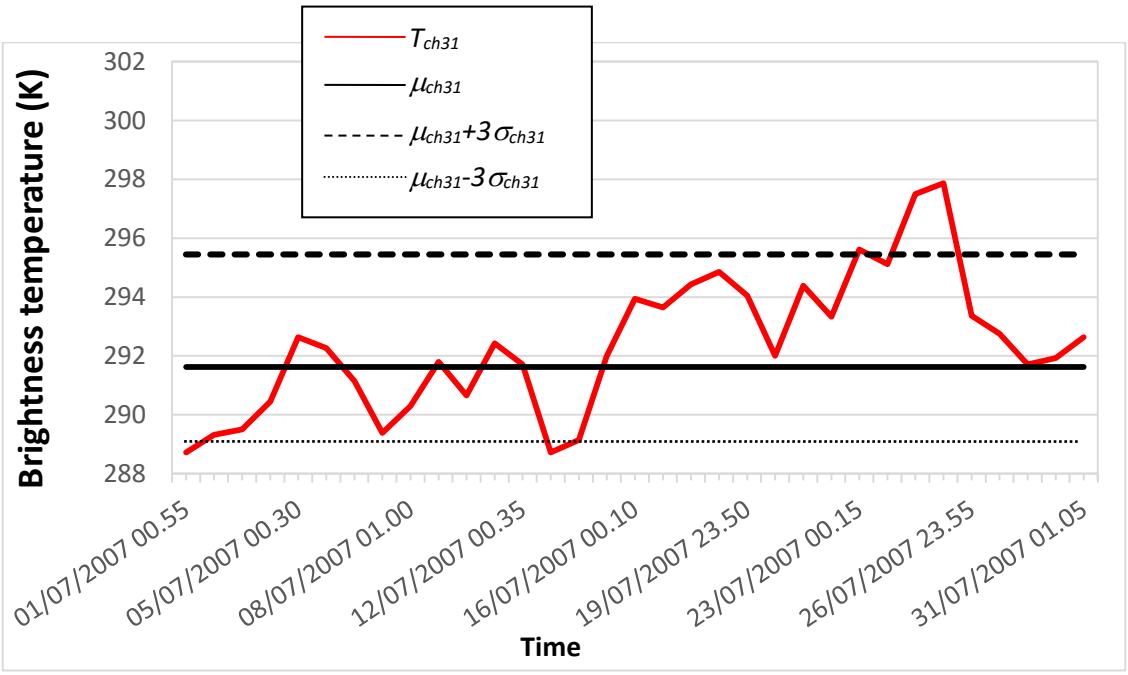

Figure 4.21: TIR signal (T_{ch31}) measured by MODIS instrument onboard Aqua platform in channel 31 during July 2007 nighttime passages over an area affected by a false alarm proliferation (MODIS pixel centered at 36.235 N, 22.985 E), together with the expected value (μ_{ch31}) and its normal variability ($\mu_{ch31} \pm 3\sigma_{ch31}$) over the same area, in the same period of the year and time of the day. Mean and standard deviation were computed on the basis of a historical dataset of nighttime MODIS/Aqua images from 2003 to 2015. The high values at the end of July are concomitant with the heat wave which affected Greece in the last decade of July 2007.

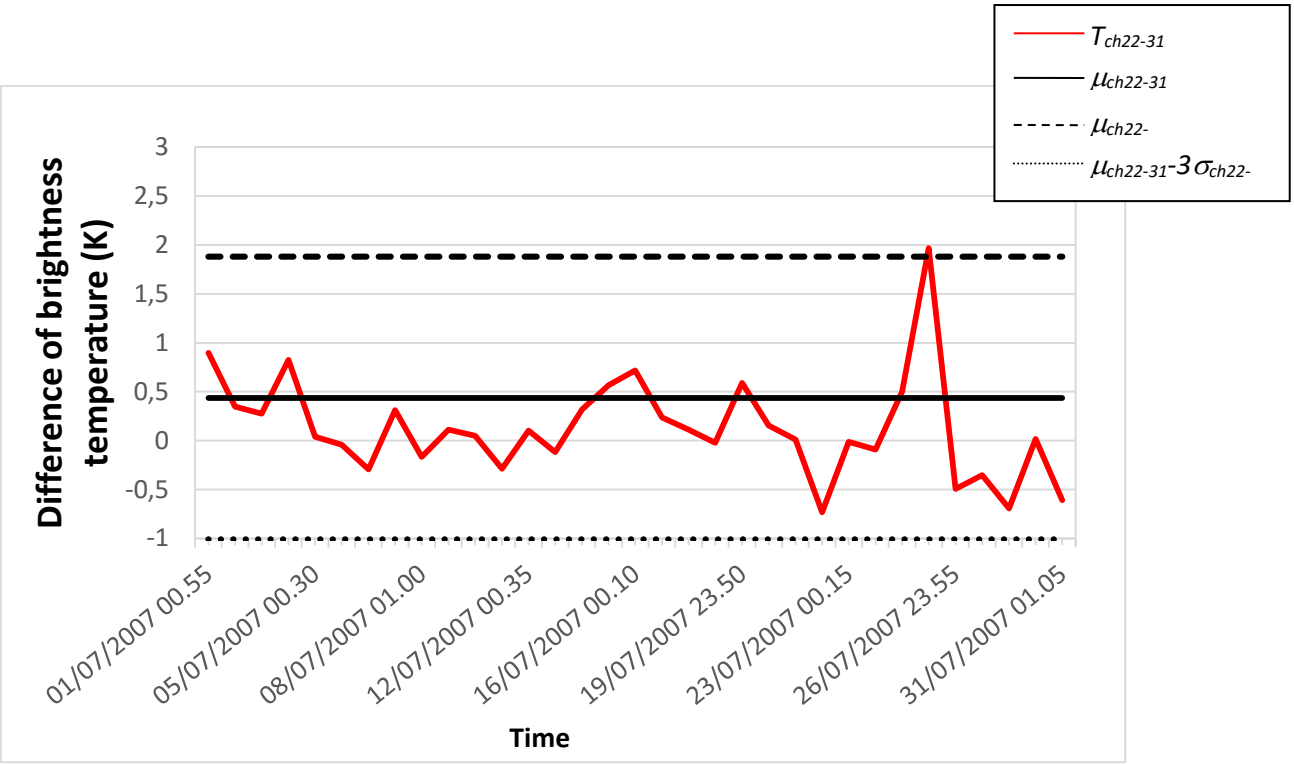

Figure 4.22: Difference of signal between MIR (channel 22) and TIR (channel 31) measured by MODIS instrument onboard Aqua platform during July nighttime passages over an area affected by false alarm proliferation (MODIS pixel centered at 36.235 N, 22.985 E), together with the expected value (Mean, $\mu_{ch22-31}$) and its normal variability (Mean ± 3 St. Dev., $\mu_{ch22-31} \pm 3\sigma_{ch22-31}$) over the same area, in the same period of the year and time of the day. Mean and standard deviation were computed on the basis of a historical dataset of nighttime MODIS/Aqua images from 2003 to 2015. The test based on $\otimes_{ch22-31}$ seems to protect from false alarm proliferation in most of the cases, but it is not enough in case of very extreme warming (see, for example, on 26 July).

4.5 Possible future developments to further improve the RST-FIRES algorithm

The RST-FIRES showed to have a good trade-off between sensitivity and reliability in detecting fires, except during the days affected by the heat wave, which any case represents a rare phenomenon.

However, the problem of a meteorological warming could be overcome by using a contextual test that in other fields of the RST application (e.g. monitoring of seismically active areas) already showed both to increase sensitivity and to protect from false alarm proliferation at the same time. The following ALICE index could be used in the case of fire detection:

$$\otimes_{\Delta s}(x,y,t,L) \equiv \frac{\Delta T_{\Delta s}(x,y,t,L) - \mu_{\Delta s}(x,y,L)}{\sigma_{\Delta s}(x,y,L)}$$

Where the satellite signal is $V(x, y, t) = \Delta T_{\Delta s}(x, y, t, L) = T_{ch22}(x, y, t) - \langle T_{ch22}(x, y, t, L)\rangle$, where $\langle T_{ch22}(x, y, t, L)\rangle$ is the mean value of $T_{ch22}(x, y, t)$ within an $L \times L$ window around the location (x,

y). $<T_{ch22}(x, y, t, L)>$ is computed excluding the pixel under evaluation (x, y), its nearest neighbours, and all of the remaining (NC) cloudy pixels. Therefore, $<T_{ch22}(x, y, t, L)>$is computed on a number of cloud-free pixels as

$$NUMWIN = L \times L - 9 - NC.$$

Figure 4.23 shows this spatial differential signal $\Delta T_{\Delta s}$ (where L=9) together with the expected value ($\mu_{\Delta s}$) and its normal variability ($\mu_{\Delta s} \pm 2\ \sigma_{\Delta s}$) over the same area (same MODIS pixel), in the same period of the year, and time of the day as Figure , Figure , and Figure .

As expected, unlike MIR, TIR, MIR-TIR signals, the differential signal, $\Delta T_{\Delta s}$ seems not to be affected by the heat wave.

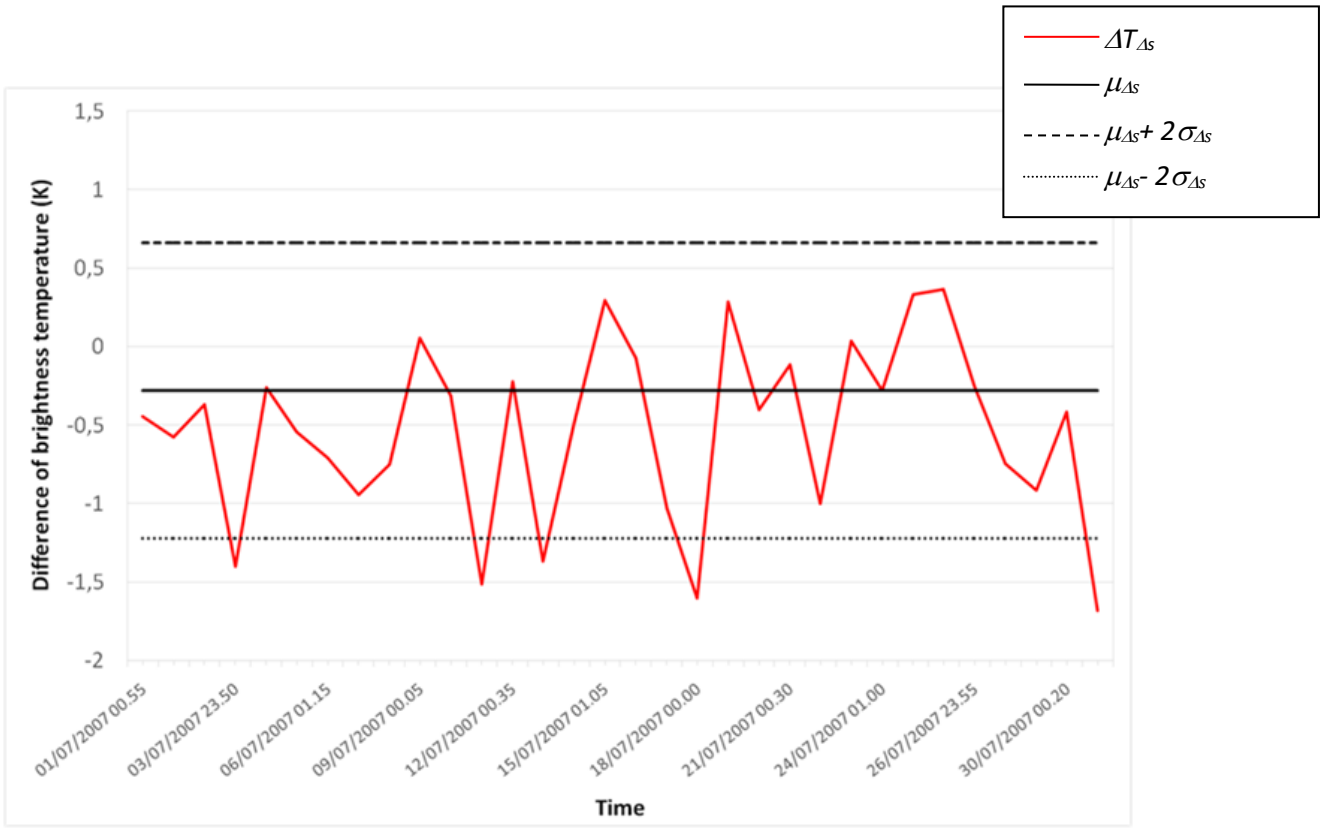

Figure 4.23: Difference of signal between MIR (channel 22) in MODIS pixel centred at 36.235 N, 22.985 E and the spatial mean measured in the 9 x 9 window around the central pixel. The spatial mean is measured excluding pixel under evaluation, its nearest neighbours, and all of the remaining cloudy pixels. This differential signal is shown together with the expected value ($\mu_{\Delta s}$) and its normal variability ($\mu_{\Delta s} \pm 2\sigma_{\Delta s}$). Mean and standard deviation were computed on the basis of a historical dataset of night time MODIS/Aqua images from 2003 to 2015.

In addition, the use of the differential $\otimes_{\Delta s}$ index, for example in combination with $\otimes_{ch22\text{-}31}$, could improve RST-FIRES performance also in terms of sensitivity. A preliminary use of this index was done in the case (before described) of the fire occurred in the Prefecture of Rethymno on 2 July

2007. As already seen (Figure), the present RST-FIRES configuration, based on the $\otimes_{ch22}$ ($\otimes_{ch21}$) and$\otimes_{ch22-31}$($\otimes_{ch21-31}$) indices, is not able to identify any thermal anomaly in correspondence to the fire. On the contrary, an index based on the differential signal $\Delta T_{\Delta s}$ would enable the detection of the fire, showing values up to 10 (Figure 4.24).

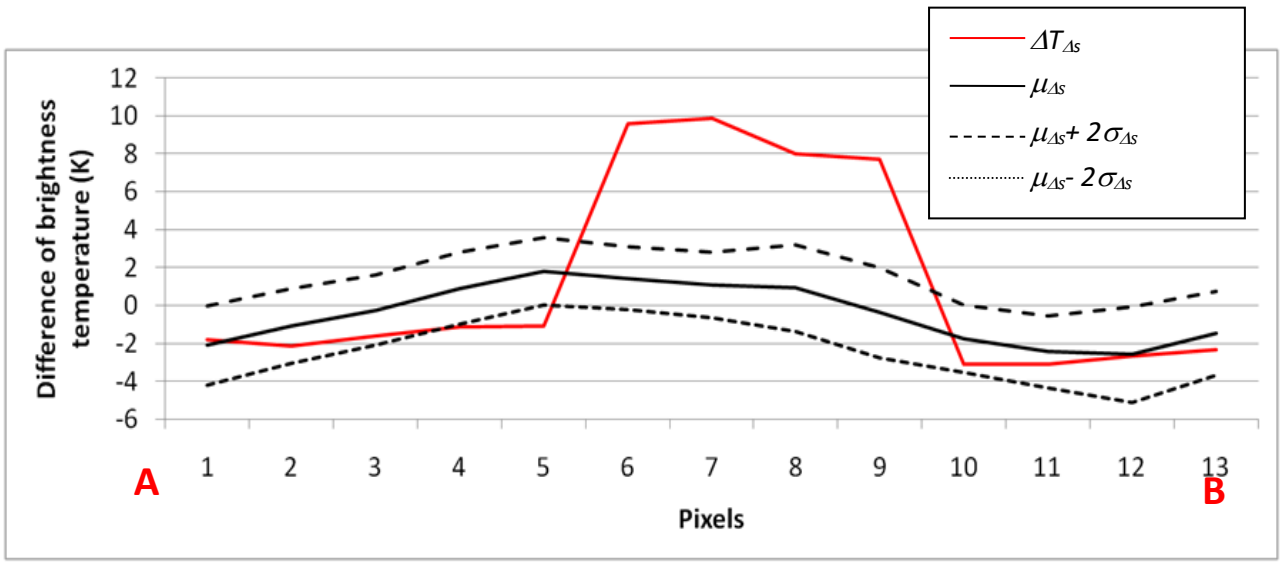

Figure 4.24: Fire in the Prefecture of Rethymno (2 July 2007). The differential signal, $\Delta T_{\Delta s}$, compared with the expected value ($\mu_{\Delta s}$) and its normal variability ($\mu_{\Delta s} \pm 2\sigma_{\Delta s}$), along the same transect as Figure a. It is evident that an index based on such a signal, also in combination with $\otimes_{ch22-31}$, would enable to detect the fire which the present RST-FIRES configuration fails to identify. The signal excess ($\Delta T_{\Delta s}$ - $\mu_{\Delta s}$) is up to 10 times standard deviation $\sigma_{\Delta s.}$

Conclusion

The forest is one of the most complex systems in the nature. Forest fires in this complex system represent serious problems, mainly for a natural point of view, but also for the society and the economy. For this reason fires should be detected as soon as possible. In such a framework remote sensing data, thanks to the capability to cover large areas with high temporal frequency and relatively low cost, may provide a useful support.

In this thesis RST and MOD14/MYD14 algorithms approach, was applied to MODIS for fire forest detection and investigation. The study was focalized on Crete Island and Attica. For the study area 10.468 images (34 Gbytes) covering the period 2003-20015 was analysed. After that, from the data, July 2007 selected for the analysis because it was one of the biggest disasters in Greece, especially in Attica. MSG-SEVIRI sensor data also used, in a case for the confirmation of fire signal. Specifically the validation of RST-FIRES algorithm was performed on the basis of 194 document events (for Attica and Crete). In many of these cases (about 45%) fire position was not possible so clear and it was not possible to perform the sensitivity analysis for such a fire. Nevertheless, presented a high degree of fire detection, about 30% were succefully identified by RST-FIRES.

The percentages for the 194(Attica=69 and Crete=125) documented fires with known and unknown position are the following:

1. Documented fires with unknown position: 88 (30%) (Attica=28 and Crete= 60)
2. Documented fires with known position: 106 (55%) (Attica=41 and Crete=65) from which:

Not observable fires: 43 (Attica=15, Crete=28)

- Fires not observable due to cloud cover: 2 (Attica=1, Crete=1)
- Fires not observable due to lack of MODIS passages: 41 (Attica=14, Crete=27)

Observable fires: 63 (Attica=26, Crete=37)

- Detected fires: 19 (30%) (Attica=8, Crete=11)
- Undetected fires: 44(70%) (Attica= 18, Crete=26). Specifically 43 was not evident spatial signal variation (Attica=18, Crete=25) and 1 (Crete) was algorithms related reason

Moreover RST-FIRES were compared with MOD14/MYD14 which is the most used MODIS-based fire detection at global level. The results from the observable fires (Attica=26, Crete=37) that came out were the followings:

RST-FIRES

- 8(31%) identified events for Attica and 7(30%) identified events for Crete
- Thermal anomalies associated to events: 62 for Attica and 42 for Crete
- Thermal anomalies not associated to events: 71 for Attica and 39 for Crete

MOD14/MYD14

- 7(27%) identified events for Attica and 9(24%) identified events for Crete
- Thermal anomalies associated to events: 28 for Attica and 39 for Crete
- Thermal anomalies not associated to events: 1 for Attica and 0 for Crete

On the whole, RST-FIRES even with the present configuration showed to have a good trade-off between sensitivity and reliability. Anyway, as shown in a preliminary way in the section 4.5, the use of a differential index (in a possible combination with already used indices) could further improve the RST-FIRES performance both in sensitivity and reliability. The combination between high sensitivity and reliability could be exploited to successful identify fires before they dangerously spread over large areas so to avoid disasters like the ones sorrowfully registered in July 2007 in Greece.

References

- Nicolaos I. Sifakis , Christos Iossifidis , Charalabos Kontoes and Iphigenia Keramitsoglou , Wildfire Detection and Tracking over Greece Using MSG-SEVIRI Satellite Data , Remote Sens. 2011.
- Andrea Camia, Jesús San-Miguel-Ayanz, Jan Kucera, Giuseppe Amatulli, Roberto Boca, Giorgio, Forest Fires in Europe 2007 , EUR 23492 EN – Joint Research Centre – Institute for Environment and Sustainability, Luxembourg: Office for Official Publications of the European Communities 2008
- ΑθανασίουΜιλτιάδης, ΞανθόπουλοςΓαβριήλ, Ησυμπεριφοράτωνμεγάλωνδασικώνπυρκαγιώντου 2007 στηνΕλλάδα,ΕθνικόΙδρυμαΑγροτικώνΕρευνώνΙνστιτούτοΜεσογειακώνΔασικώνΟικοσυστημάτωνκαιΤεχνολογίαςΔασικώνΠροϊόντων
- M BARNSLEY, Digital remotely-sensed data and their characteristics,ch32, Remote Sensing, Chapter 2
- Wow CD-ROM Handout 2, Introduction to Remote Sensing , February 1999
- Shefali Aggarwal, PRINCIPLES OF REMOTE SENSING, Photogrammetry and Remote Sensing Division, Indian Institute of Remote Sensing, Dehra Dun
- INTRODUCTION TO REMOTE SENSING, *Paul R. Baumann,* © 2010 Paul R. Baumann
- National Aeronautics and Space Administration, Tour of the Electromagnetic Spectrum, NP-2010-07-664-HQ
- C.O. JUSTICE, J.-P. MALINGREAU and A.W. SETZER, Satellite Remote Sensing of Fires: Potential and Limitations, Fire in the Enwronment: The Ecological, A tmospheric, and Climatic Importance of Vegetation Fires Edited by P.J. Crutzen and J.G. Goldammer @ 1993 John Wiley& Sons Ltd.
- Abel Calle and José Luis Casanova (2012). Forest Fires and Remote Sensing, Earth Observation
- Abel Calle and José Luis Casanova (2012). Forest Fires and Remote Sensing, Earth Observation,
- Tawanda Manyangadze, March 2009, Forest fire detection for near real-time monitoring using geostationary satellites
- SUSAN PHILIP MARCH, 2007, ACTIVE FIRE DETECTION USING REMOTE SENSING BASED POLAR-ORBITING AND GEOSTATIONARY OBSERVATIONS: AN APPROACH TOWARDS NEAR REAL-TIME FIRE MONITORING
- Giuseppe Mazzeo, Francesco Marchese, Carolina Filizzola, Nicola Pergola, Valerio Tramutoli, A Multi-temporal Robust Satellite Technique (RST) for Forest Fire Detection,©2007 IEEE,

- Carolina Filizzola, Rosita Corrado, Francesco Marchese, Giuseppe Mazzeo, Rossana Paciello, Nicola Pergola, Valerio Tramutoli, RST-FIRES, an exportable algorithm for early-fire detection and monitoring: description, implementation, andfieldvalidationinthecaseoftheMSG-SEVIRIsensor
- Tramutoli V, (1998). Robust AVHRR techniques (RAT) for environmental monitoring: theory and applications, Earth surface remote sensing II. Proceeding of SPIE, 3496, 101-113.
- Tramutoli V. (2007). Robust Satellite Techniques (RST) for Natural and Environmental Hazards Monitoring and Mitigation: Theory and Applications, Proceeding of Multitemp 2007, doi
- Christopher O. Justice, Louis Giglio, David Roy, Luigi Boschetti, Ivan Csiszar, Diane Davies, Stefania Korontzi, W. Schroeder, Kelley O'Neal, and Jeff Morisette, MODIS-Derived Global Fire Products, B. Ramachandran et al. (eds.), Land Remote Sensing and Global Environmental Change, Remote Sensing and Digital Image Processing 11, DOI 10.1007/978-1-4419-6749-7_29, © Springer Science+Business Media, LLC 2011
- LouisGiglio, MODISCollection5ActiveFireProductUser'sGuide Version2.4, 18February2010
- C.O. Justice, L. Giglio, S. Korontzi, J. Owens, J.T. Morisette, D. Roy, J. Descloitres, S. Alleaume, F. Petitcolin, Y. Kaufman, The MODIS fire products, Remote Sensing of Environment 83 (2002) 244–262
- Junpen A., Garivait S., Bonnet S., and Pongpullponsak A, Spatial and Temporal Distribution of Forest Fire PM10 Emission Estimation by Using Remote Sensing Information
- Yrjö Rauste, FOREST FIRE DETECTION WITH SATELLITES FOR FIRE CONTROL, International Archives of Photogrammetry and Remote Sensing. Vol XXXI, Part B7. Vienna 1996
- Theoharatos, G., Pantavou, K., Mavrakis, A., Spanou, A., Katavoutas, G., Efstathiou, P., Mpekas, P., Asimakopoulos, D. (2010). Heat waves observed in 2007 in Athens, Greece: Synoptic conditions, bio climatological assessment, air quality levels and health effects. Environmental Research, Vol. 110, Issue 2, pp. 152–161, doi:10.1016/j.envres.2009.12.002
- Tolika, K., Maheras, P., Tegoulia, I. (2009). Extreme temperatures in Greece during 2007: Could this be a ‘‘return to the future’ ’Geophysical Research Letters, vol. 36, L10813, doi:10.1029/2009GL038538
- Land Care in Desertification Affected Areas, Science Towards Application, Ramon Vallejo, Alejandro Valdecantos.

Web References

- file:///H:/chapter1/10031.pdf
- http://www.conserve-energy-future.com/causes-effects-and-solutions-of-wildfires.php
- http://eschooltoday.com/natural-disasters/wildfires/wildfire-facts.html
- https://en.wikipedia.org/wiki/2007_Greek_forest_fires
- file:///H:/chapter2/remotesensing/remote_sensing_chap5.pdf
- http://www.satimagingcorp.com/services/resources/characterization-of-satellite-remote-sensing-systems/
- https://en.wikipedia.org/wiki/Remote_sensing

- http://www.emodnet-seabedhabitats.eu/default.aspx?page=1815
- http://www.crisp.nus.edu.sg/~research/tutorial/spacebrn.htm
- http://www.crisp.nus.edu.sg/~research/tutorial/intro.htm
- http://earthobservatory.nasa.gov/Features/GlobalFire/fire_5.php
- https://en.wikipedia.org/wiki/Advanced_Spaceborne_Thermal_Emission_and_Reflection_Radiometer
- http://science.nasa.gov/missions/goes-r/
- http://www.goes-r.gov/education/docs/Factsheet_FireDetection_Feb2014.pdf
- http://noaasis.noaa.gov/NOAASIS/ml/genlsatl.html
- https://www.class.ngdc.noaa.gov/data_available/goes/index.htm
- file:///C:/Users/prova/AppData/Local/Temp/78889.pdf
- http://www.ga.gov.au/scientific-topics/earth-obs/satellites-and-sensors/modis
- https://earthdata.nasa.gov/firms-faq
- http://eoweb.dlr.de:8080/short_guide/D-MODIS.html
- http://www.ekdd.gr/ekdda/files/ergasies_esta/T1/030/10031.pdf
- http://eclass.teiion.gr/modules/document/file.php/ECO128/%CE%A3%CE%B7%CE%BC%CE%B5%CE%B9%CF%8E%CF%83%CE%B5%CE%B9%CF%82%20%CE%B1%CF%80%CF%8C%20%CE%94%CE%B9%CE%B1%CE%B4%CE%AF%CE%BA%CF%84%CF%85%CE%BF/%CE%A0%CF%85%CF%81%CE%BA%CE%B1%CE%B3%CE%B9%CE%AD%CF%82_Final_GR.pdf